A Rhombic Planform Nonlinear Stability Analysis of a Noncytopathic EIAV-Target Cell Limited Interaction-Dispersion-Chemotaxis Quasi-Equilibrium Model System

David J. Wollkind[*] & Bonni Dichone[†]

Abstract

A noncytopathic EIAV-target cell limited interaction dynamical model system is extended by including the spatial effects of dispersion and chemotaxis. A linear stability analysis of its two equilibrium states and both one-dimensional longitudinal and two-dimensional rhombic planform nonlinear stability analyses of the infectious one are performed on a quasi-equilibrium version of this model system. That system only depends on two dimensionless ratios: The basic reproductive number and a chemotaxis coefficient, which is a measure of the attraction of the uninfected target cells to density gradients in the infected target cells. For sufficiently large values of the chemotaxis coefficient, a morphological infection sequence of the uninfected state to sparse homogeneous distributions and isolated spots to periodic spots to dense homogeneous distributions is predicted as the basic reproductive number increases from zero. Then, the patterned region is identified with the occurrence of petechial hemorrhages or minute blood-red spots on the anemic mucous membranes of horses during the chronic degree phase of EIAV infectiousness. The concept of higher threshold rhombic patterns based on the mean density deviation level of the infected target cells is introduced to make the interpretation of spots in the periodic patterning region. The distance between these adjacent spots decreases as the basic reproductive number increases, consistent with this predicted morphological infection sequence.

Keywords: Virus-Horse Dynamics; Spatial Diffusion Effects; Equilibrium Approximation; Turing Instabilities; Spots versus Stripes; Petechiation Patterns.

1 Introduction and Formulation of the Problem

In order to examine the HIV (human immunodeficiency virus) infection, Anderson and May [1] proposed a basic three-component dynamical model system consisting of an uninfected target cell population, an infected such population, and the free virus. This model implied that the propagation of the virus was limited by the availability of susceptible target cells and hence is now characterized as target cell-limited (Phillips, [20]). Assuming a rapid enough time-scale for the free

---

[*]Department of Mathematics, Washington State University, Pullman, WA 99164-3113, USA
[†]Department of Mathematics, Gonzaga University, 502 E. Boone Avenue MSC 2615, Spokane, WA 99258, USA

virus dynamics so that a quasi-steady-state approximation could be employed, Tuckwell and Wan [25] formally reduced this basic target cell-limited viral model system to a two-component one consisting of the uninfected and infected target cells. Defining $\alpha = \rho/\delta \equiv$ the ratio of the death rates of the uninfected to the infected target cells, Burg *et al.* [3] classified such an interaction to be either cytopathic or noncytopathic depending upon whether $\alpha < 1$ or $\alpha = 1$, respectively. For cytopathic viral interactions, the target cells are killed during the course of infection. In noncytopathic ones, they are not. That is the case for the target cell limited EIAV (equine infectious anemia virus) interaction (Schwartz *et al.*, [21]) which we shall be modeling. It is unusual among lentiviruses, in that most infected animals, after a few episodes of fever and high viral load, progress to a chronic degree phase. The horses effectively control viral replication through adaptive immune mechanisms. When adopting the dynamical system of Anderson and May [1], the viral clearance rate γ implicitly captures these adaptive immune system response mechanisms. Since typically $\varepsilon = \rho/\gamma = O(10^{-3})$ for EIAV, Cangelosi *et al.* [4] put the quasi-steady-state assumption introduced by Tuckwell and Wan [25] on a firm mathematical foundation for a noncytopathic system by employing the two-time Matkowsky method [17] to deduce an asymptotic closed-form analytical solution of that basic target-cell-limited viral interaction model. These references involved ordinary differential equation models that assumed the target-cell populations and the free virus were homogeneously distributed in space. Hence their densities and concentration were functions of time alone. Stancevic *et al.* [24] relaxed this assumption by considering an interaction-dispersion-chemotaxis three-component in-host viral partial differential equation model system for the densities of uninfected and infected target cells and the concentration of a cytopathic virus which were heterogeneous functions of their transverse spatial coordinates, as well as of time. They found that the cross-diffusive effect of chemotaxis toward the infected cells by the uninfected ones generated their pattern formation instability in a similar manner as root suction did for the two-component plant-ground water system of Chaiya *et al.* [6]. This mechanism was analogous in form to the one relevant to the slime-mold chemotaxis model of Keller and Segel [13]. In what follows, we shall introduce a spatial extension of that sort for the basic target-cell-limited noncytopathic viral dynamical model system investigated by Cangelosi *et al.* [4] to explain more fully the petechial hemorrhages or minute blood-red spotted patterns that can appear on the anemic equine mucous membranes during the chronic degree phase of EIAV infectiousness. That is, after Cangelosi *et al.* [4] and Stancevic *et al.* [24], we consider:

$$\frac{\partial T}{\partial \tau} = \lambda - \rho T - \beta T V + D_1 \nabla_2^2 T - \chi_1 \boldsymbol{\nabla}_2 \cdot (T \boldsymbol{\nabla}_2 I), \tag{1.1a}$$

$$\frac{\partial I}{\partial \tau} = \beta T V - \delta I + D_2 \nabla_2^2 I, \quad \frac{\partial V}{\partial \tau} = bI - \gamma V + D_3 \nabla_2^2 V; \tag{1.1b,c}$$

where $\boldsymbol{\nabla}_2 \equiv \left(\frac{\partial}{\partial r_1}, \frac{\partial}{\partial r_2} \right)$ and $\nabla_2^2 = \boldsymbol{\nabla}_2 \cdot \boldsymbol{\nabla}_2$ with $\delta = \rho$ and $D_2 = D_1$. \hfill (1.1b)

Here $T \equiv$ uninfected target cell population density (cells/ml), $I \equiv$ infected target cell population density (cells/ml), and $V \equiv$ free virus particle concentration (viral RNA copies/ml), where we are now assuming the densities of T and I cells and the concentration of our noncytopathic V particles to be heterogeneous functions of their transverse spatial coordinates (r_1, r_2), measured in mm $\equiv$ millimeters, on an anemic equine mucous membrane of infinite planar extent, as well as functions of time τ, measured in days. Further, it is assumed that T cells are produced at a constant rate λ and die at a rate ρT; V particles infect T cells at a rate $\beta T V$; I cells die at a
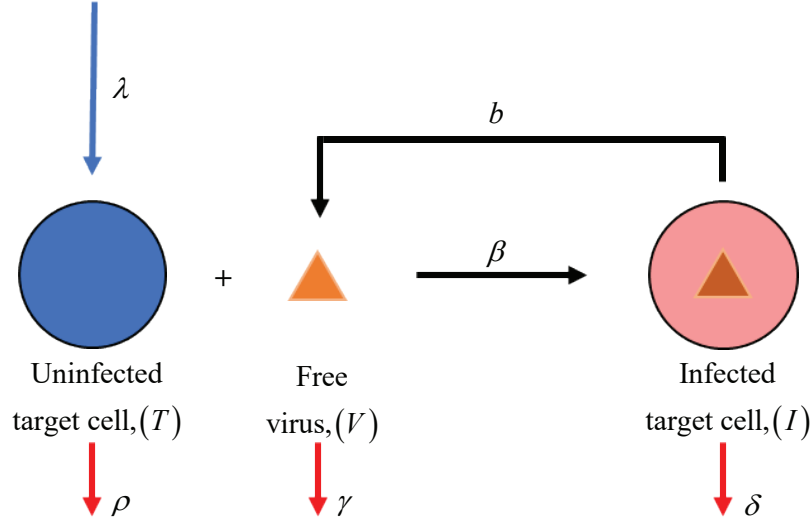
Figure 1.1: Schematic diagram of the interaction terms of the dimensional EIAV-target cell limited interaction-dispersion-chemotaxis model system (Cangelosi *et al.*, [4]). Uninfected target cells (T) can be infected by the free virus (V) to create infected target cells (I). In the case of a noncytopathic virus like EIAV, $\alpha = \rho/\delta = 1$ or $\delta = \rho$.

rate δI ($\delta = \rho$); and V particles are produced at a rate bI and cleared at a rate γV (see Fig. 1.1); while T, I, and V disperse with dispersal coefficients D_1, D_2, and D_3, respectively, where for simplicity this motility is identified with Brownian motion; T and I cells both disperse at the same rate ($D_2 = D_1$); and, finally, T cells are chemotactically attracted to, and move toward, density gradients in I cells with strength χ_1 (see Table 1.1) since the latter recruit the former by signaling them through the release of chemokines (chemotactic cytokines) producing inflammation at the site of the infection (Stancevic *et al.*, [24]), which appears as petechial hemorrhages or petechiations on the anemic mucous membranes of horses during the chronic degree phase of EIAV infectiousness (fs_equine_infectious_anemia.pdf; APHIS Factsheet, 2008).

Introducing the nondimensional variables (Wollkind and Dichone, [31])

$$(x, y) = \frac{(r_1, r_2)}{\sqrt{D_1/\rho}}, \ t = \rho\tau; \ m = \frac{\rho T}{\lambda}, \ i = \frac{\rho I}{\lambda}, \ v = \frac{\beta V}{\rho}; \tag{1.2}$$

our equations become

$$\frac{\partial m}{\partial t} = 1 - m - mv + \nabla^2 m - \chi \boldsymbol{\nabla} \cdot (m\boldsymbol{\nabla} i) \text{ where } \chi = \frac{\lambda \chi_1}{\rho D_1}, \tag{1.3a}$$

$$\alpha\frac{\partial i}{\partial t} = mv - i + \nabla^2 i \text{ where } \alpha = \frac{\rho}{\delta} = 1, \tag{1.3b}$$

$$\varepsilon\frac{\partial v}{\partial t} = R_0 i - v + \varepsilon\mu\nabla^2 v \text{ where } \varepsilon = \frac{\rho}{\gamma}, \ R_0 = \frac{\lambda\beta b}{\rho\delta\gamma} = \frac{\lambda\beta b}{\rho^2\gamma}, \text{ and } \mu = \frac{D_3}{D_1}. \tag{1.3c}$$

3

Model parameter	Units	Description
λ	cells/(ml $\times$ day)	Source rate of T
β	ml/(viral RNA copies $\times$ day)	Infection rate of T
b	viral RNA copies/(cells $\times$ day)	Production rate of V
ρ	1/day	Death rate of T
δ	1/day	Death rate of I
γ	1/day	Clearance rate of V
D_1	mm^2/day	Dispersal coefficient of T
D_2	mm^2/day	Dispersal coefficient of I
D_3	mm^2/day	Dispersal coefficient of V
χ_1	mm$^2 \times$ ml/(cells $\times$ day)	Chemotactic strength

Table 1.1: Units and description of model parameters. Here, ml $\equiv$ milliliter and RNA $\equiv$ ribonucleic acid present in a virus that carries its genetic information. Note that the dimensions of $\lambda\beta b$ and $\rho\delta\gamma$ are both 1/day^3 while those of $\lambda\chi_1$ and ρD_1 are both mm^2/day^2. Thus the basic reproductive number R_0 and chemotaxis coefficient χ (see below) are dimensionless ratios.

Then, as can be seen from Table 1.2, these dissipation rates and dispersal coefficients have the typical ratios of $\varepsilon = 0.007$ and $\mu = 0.008$, respectively. The fact that the very small parameter ε of Cangelosi *et al.* [4] appears as a factor in the viral equation (1.3c) dispersion term times μ, which is of the same order of magnitude, more than allows us to employ a quasi-equilibrium approximation and obtain the algebraic relation $v = R_0 i$ from this equation (see Section 2). Under these conditions, our basic equations (1.3a,1.3b) reduce to the two-component system

$$\frac{\partial m}{\partial t} = 1 - m - R_0 m i + \nabla^2 m - \chi \boldsymbol{\nabla} \cdot (m\boldsymbol{\nabla} i), \ \frac{\partial i}{\partial t} = R_0 m i - i + \nabla^2 i; \qquad (1.4\text{a,b})$$

where $\boldsymbol{\nabla} \equiv (\partial/\partial x, \partial/\partial y)$ and $\nabla^2 \equiv \boldsymbol{\nabla} \cdot \boldsymbol{\nabla}$; which only depends upon the basic reproductive number R_0 and the chemotaxis coefficient χ. Such a system is intrinsically much simpler to analyze than the three-component one treated by Stancevic *et al.* [24]. The reason for this is that the secular equation produced by a linear stability analysis of our two-component system is a quadratic, as opposed to the associated cubic equation which had to be examined by the latter authors since the Routh-Hurwitz criteria for such cubics are much more complex than the relatively simple ones for a quadratic (Uspensky, [27]). In the next section, we shall determine both equilibrium solutions for this system and perform a linear stability analysis on each of them. We shall also demonstrate conclusively the validity of our quasi-equilibrium approximation by performing a linear stability analysis on an equilibrium point of the unreduced ε-μ dependent system (1.3). Having justified that approximation in the context of diffusive instability theory, we shall perform longitudinal and rhombic planform nonlinear stability analyses of the infectious solution to our two-component quasi-equilibrium model system (1.4) in Sections 3 and 4, respectively, and close by making interpretations, applications, and comparisons of these results to EIAV-target cell limited interactions, in concluding Section 5. For those developments in these sections, we have tried to provide sufficient detail to make them reasonably self-contained.

4

Model parameter	Assigned value
λ	2019 cells/(ml $\times$ day)
β	3.25×10^{-7} ml/(viral RNA copies $\times$ day)
$\rho = \delta$	1/21 per day
γ	6.73 per day
$D_1 = D_2$	0.09504 mm^2/day
D_3	0.00076 mm^2/day

Table 1.2: The rate parameter median values reported by Schwartz *et al.* [21] for their EIAV-horse interactions and dispersal coefficients reported by Stancevic *et al.* [24]. These values correspond to $\varepsilon = \rho/\gamma = 0.007$ and $\mu = D_3/D_1 = 0.008$, while with them assigned the ratios R_0 and χ can be thought of as dimensionless versions of the parameters b and χ_1, respectively.

2 Equilibrium Points and their Linear Stability

Consider our quasi-equilibrium system for $m = m(x, y, t)$ and $i = i(x, y, t)$ written in the form:

$$\frac{\partial m}{\partial t} = F_1(m, i; R_0) + \nabla^2 m - \chi \boldsymbol{\nabla} \cdot (m \boldsymbol{\nabla} i), \tag{2.1a}$$

$$\frac{\partial i}{\partial t} = F_2(m, i; R_0) + \nabla^2 i; \tag{2.1b}$$

where

$$F_1(m, i; R_0) = 1 - m - R_0 m i, \tag{2.1c}$$

$$F_2(m, i; R_0) = R_0 m i - i. \tag{2.1d}$$

We first seek the equilibrium points of this system satisfying

$$m(x, y, t) \equiv m_e, \ i(x, y, t) \equiv i_e \text{ with } m_e, i_e \geq 0; \tag{2.2a,b}$$

such that

$$F_1(m_e, i_e; R_0) = F_2(m_e, i_e; R_0) = 0 \tag{2.2c,d}$$

or

$$R_0 m_e i_e = 1 - m_e = i_e; \tag{2.2e,f}$$

which implies the conservation of target cell equilibrium condition

$$m_e + i_e = 1. \tag{2.3}$$

Then substitution of that condition into $F_1(m_e, i_e; R_0) = 0$, yields the following quadratic in m_e:

$$R_0 m_e^2 - (R_0 + 1) m_e + 1 = 0. \tag{2.4a}$$

Factoring this quadratic into

$$(R_0 m_e - 1)(m_e - 1) = 0, \tag{2.4b}$$

we obtain its roots

$$m_e = 1 \text{ or } m_e = \frac{1}{R_0}; \tag{2.5a}$$

5

which, employing our target cell equilibrium conservation condition (2.3), results in the corresponding values of i_e:

$$i_e = 0 \text{ or } i_e = 1 - \frac{1}{R_0} = \frac{R_0 - 1}{R_0} > 0. \tag{2.5b}$$

Hence, we have deduced that there are two equilibrium points for our system given by:

$$(m_e, i_e) = (1, 0) \text{ or } (m_e, i_e) = \left(\frac{1}{R_0}, \frac{R_0 - 1}{R_0} \right) \text{ where } R_0 > 1. \tag{2.5c}$$

It is the linear stability of these equilibrium points with which we are concerned in what follows.

We begin by considering a one-dimensional linear stability solution of our system of the form

$$[m, i](x, y, t) = [m_e, i_e] + \varepsilon_1 [m_{11}, i_{11}] \cos(qx) e^{\sigma t} + \boldsymbol{O}(\varepsilon_1^2) \tag{2.6a}$$

where

$$|\varepsilon_1| \ll 1 \text{ and } |m_{11}|^2 + |i_{11}|^2 \neq 0. \tag{2.6b}$$

Noting that

$$mi = m_e i_e + \varepsilon_1 (m_e i_{11} + i_e m_{11}) \cos(qx) e^{\sigma t} + O(\varepsilon_1^2), \tag{2.7}$$

this yields a set of linear homogeneous algebraic equations in the constants m_{11} and i_{11} after substitution into system (2.1), neglect of terms of $O(\varepsilon_1^2)$, and cancellation of the common factor:

$$(\sigma + 1 + R_0 i_e + q^2) m_{11} + m_e (R_0 - \chi q^2) i_{11} = 0, \tag{2.8a}$$

$$-R_0 i_e m_{11} + (\sigma + 1 - R_0 m_e + q^2) i_{11} = 0; \tag{2.8b}$$

which, upon imposition of the vanishing of the determinant of the matrix of its coefficients to guarantee the nontriviality property for these constants, results in the following quadratic in σ:

$$(\sigma + 1 + R_0 i_e + q^2)(\sigma + 1 - R_0 m_e + q^2) + R_0 i_e m_e (R_0 - \chi q^2) = 0. \tag{2.9}$$

Since Turing [26] diffusive instabilities are defined to be those solutions that are stable in the absence of spatial effects but can become unstable if these effects are taken into account, we first examine the behavior of this quadratic in their absence or equivalently for $q^2 \equiv 0$. Then

$$(\sigma + 1 + R_0 i_e)(\sigma + 1 - R_0 m_e) + R_0^2 i_e m_e = 0. \tag{2.10a}$$

We shall investigate this behavior for each equilibrium point sequentially:

For the uninfected equilibrium point $m_e = 1$ and $i_e = 0$, we obtain

$$(\sigma + 1)(\sigma + 1 - R_0) = 0 \Rightarrow \sigma_1 = -1 \text{ and } \sigma_2 = R_0 - 1. \tag{2.10b}$$

Then there will be stability provided that $\sigma_{1,2} < 0$ or $0 < R_0 < 1$.

For the community equilibrium point $m_e = 1/R_0$ and $i_e = (R_0 - 1)/R_0 > 0$, we obtain

$$(\sigma + R_0)\sigma + R_0 - 1 = \sigma^2 + R_0 \sigma + R_0 - 1 = 0. \tag{2.10c}$$
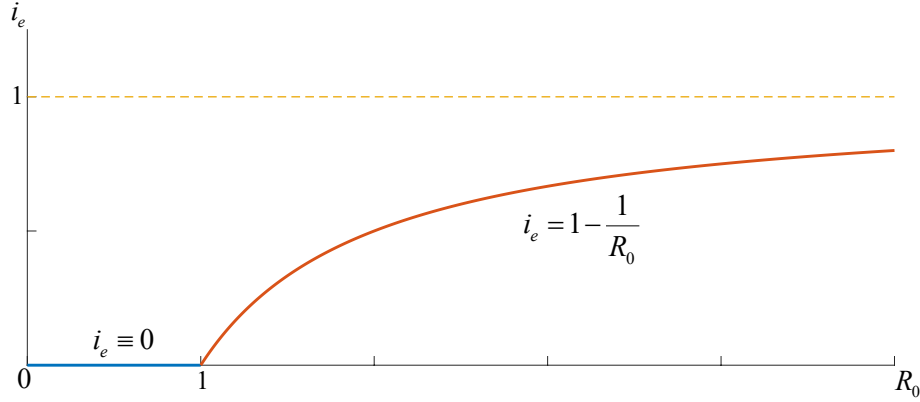
6

Figure 2.1: A plot of i_e, the infected target cell component of the equilibrium points, versus R_0, the basic reproductive number. Here $i_e \equiv 0$ for $0 < R_0 < 1$ and $i_e = 1 - 1/R_0 > 0$ represent that component for the uninfected and community equilibrium points, respectively. Note that these equilibrium points are linearly stable in the absence of spatial effects over those R_0-parameter ranges and there is an exchange of stabilities between them at $R_0 = 1$ where they are equivalent.

Recalling that given $\sigma^2 + a\sigma + c = 0$, $\text{Re}(\sigma_{1,2}) < 0$ if and only if $a, c > 0$, then there will be stability provided $R_0 > 1$, which is also the existence condition for this solution (see Fig. 2.1).

Next we examine the possibility of the occurrence of diffusive instabilities for each of these equilibrium points when spatial effects are considered or equivalently when $q^2 > 0$.

For $m_e = 1$ and $i_e = 0$, we obtain

$$(\sigma + 1 + q^2)(\sigma + 1 - R_0 + q^2) = 0 \Rightarrow \sigma_1 = -1 - q^2 \text{ and } \sigma_2 = R_0 - 1 - q^2. \tag{2.11}$$

Thus, since $\sigma_{1,2} < 0$ when $R_0 < 1$, there can be no diffusive instabilities for this solution.

For $m_e = 1/R_0$ and $i_e = (R_0 - 1)/R_0 > 0$, we obtain

$$(\sigma + R_0 + q^2)(\sigma + q^2) + (R_0 - 1)\left(1 - \frac{\chi q^2}{R_0}\right) = \sigma^2 + (2q^2 + R_0)\sigma + (R_0 + q^2)q^2 + (R_0 - 1)\left(1 - \frac{\chi q^2}{R_0}\right),$$
$$\tag{2.12a}$$

which implies that $\text{Re}(\sigma_{1,2}) < 0$ if and only if

$$(R_0 + q^2)q^2 + (R_0 - 1)\left(1 - \frac{\chi q^2}{R_0}\right) > 0. \tag{2.12b}$$

Hence there will be a Turing diffusive instability for this solution provided

$$\chi > \chi_0(q^2; R_0) = \frac{R_0}{R_0 - 1}\left(R_0 + q^2 + \frac{R_0 - 1}{q^2}\right) \text{ where } R_0 > 1 \tag{2.13}$$

and marginal stability when $\chi = \chi_0(q^2; R_0)$ which is plotted in the q^2-χ plane of Fig. 2.2. Since

$$\lim_{q^2 \to 0} \chi_0(q^2; R_0), \ \lim_{q^2 \to \infty} \chi_0(q^2; R_0) \to \infty \text{ and } \chi_0(q^2; R_0) > 0, \tag{2.14}$$
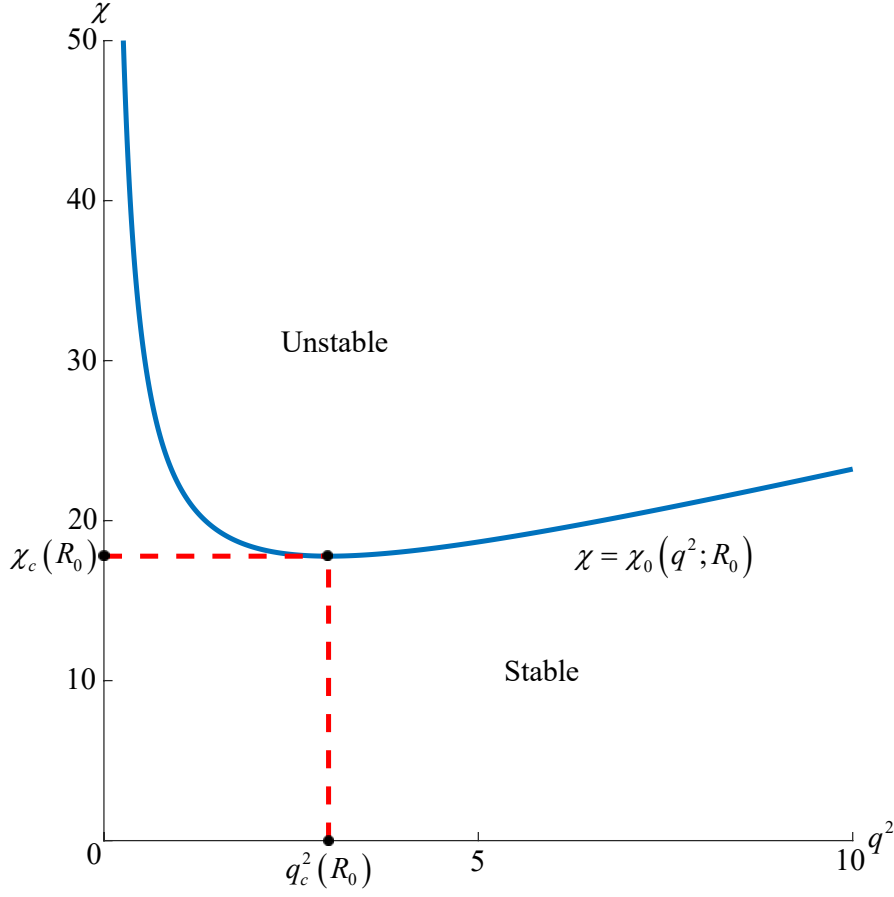
7

Figure 2.2: A plot of the marginal stability curve $\chi = \chi_0(q^2; R_0)$ in the q^2-χ plane for $R_0 = 10$, denoting the linear stability behavior for the community equilibrium point where χ is a measure of the chemotactic motion of m cells along the i-cell gradient. Here, (q_c^2, χ_c) represents the minimum point of this curve where, for $R_0 > 1$, $q_c^2(R_0) = \sqrt{R_0 - 1}$ and $\chi_c(R_0) = \chi_0(q_c^2; R_0)$.

this curve must have an absolute minimum at its critical point (q_c^2, χ_c) which satisfies

$$\frac{d\chi_0}{dq^2}(q_c^2; R_0) = 0 \implies q_c^2(R_0) = \sqrt{R_0 - 1} \text{ and } \chi_c(R_0) = \chi_0(q_c^2; R_0). \tag{2.15}$$

Hence, for $0 < \chi < \chi_c$, there exists no q^2 associated with growing modes, while for $\chi > \chi_c$ there exists a band of such wavenumbers squared centered about $q^2 = q_c^2$. Therefore, this equilibrium point is linearly stable for $0 < \chi < \chi_c$, unstable for $\chi > \chi_c$, and neutrally stable for $\chi = \chi_c$. That marginal stability function

$$\chi_c(R_0) = \frac{R_0}{R_0 - 1}(R_0 + 2\sqrt{R_0 - 1}) = \frac{R_0^2}{R_0 - 1} + \frac{2R_0}{\sqrt{R_0 - 1}} \tag{2.16}$$

is plotted in the R_0-χ plane of Fig. 2.3 for $R_0 > 1$. Again, since

$$\lim_{R_0 \to 1} \chi_c(R_0), \ \lim_{R_0 \to \infty} \chi_c(R_0) \to \infty \text{ and } \chi_c(R_0) > 0, \tag{2.17}$$

8

that curve must have an absolute minimum at its critical point which is determined as follows:

$$\chi_c'(R_0) = \frac{2R_0}{R_0 - 1} - \frac{R_0^2}{(R_0 - 1)^2} - \frac{R_0}{(R_0 - 1)^{3/2}} + \frac{2}{(R_0 - 1)^{1/2}} = \frac{F(R_0)}{(R_0 - 1)^2} \qquad (2.18a)$$

where

$$F(R_0) = 2R_0(R_0 - 1) - R_0^2 - R_0\sqrt{R_0 - 1} + 2(R_0 - 1)^{3/2} = (R_0 + \sqrt{R_0 - 1})(R_0 - 2). \qquad (2.18b)$$

Observing that $F(R_0) < 0$ for $1 < R_0 < 2$, $F(2) = 0$, $F(R_0) > 0$ for $R_0 > 2$, and $\chi_c(2) = 8$, this minimum point is located at $(2, 8)$, as indicated in Fig. 2.3, which also identifies the behavior in that plane predicted by our linear diffusive instability analysis.

Finally, let us provide a justification of our quasi-equilibrium approximation to the basic governing partial differential equations for this EIAV-target cell interaction-dispersion-chemotaxis model. Performing a linear stability analysis of its generic equilibrium point

$$m \equiv m_e, \ i \equiv i_e, \ v \equiv v_e \text{ where } i_e = 1 - m_e \text{ and } v_e = R_0 i_e \qquad (2.19)$$

on the unreduced ε-μ dependent model (1.3), we obtain the linear homogeneous algebraic system in the perturbation quantities m_{11}, i_{11}, v_{11}:

$$(\sigma + 1 + v_e + q^2)m_{11} - m_e\chi q^2 i_{11} + m_e v_{11} = 0, \qquad (2.20a)$$

$$-v_e m_{11} + (\sigma + 1 + q^2)i_{11} - m_e v_{11} = 0, \qquad (2.20b)$$

$$0m_{11} - R_0 i_{11} + (\varepsilon\sigma + 1 + \varepsilon\mu q^2)v_{11} = 0; \qquad (2.20c)$$

where $|m_{11}|^2 + |i_{11}|^2 + |v_{11}|^2 \neq 0$, which, upon imposition of the vanishing of the determinant of the matrix of its coefficients to guarantee this nontriviality property for these quantities, yields the following cubic in σ:

$$(\varepsilon\sigma + 1 + \varepsilon\mu q^2)[(\sigma + 1 + v_e + q^2)(\sigma + 1 + q^2) - m_e v_e \chi q^2] - R_0 m_e(\sigma + 1 + q^2) = 0. \qquad (2.21)$$

From this cubic we can deduce that should $\mu = O(1)$ as $\varepsilon \to 0$, there are two roots $\sigma_{1,2} = O(1)$ as $\varepsilon \to 0$ which reduce when $\varepsilon = 0$ to those just examined for the linear stability analysis of the quasi-equilibrium system, while its third root $\sigma_3 \sim -1/\varepsilon$ as $\varepsilon \to 0$. Thus, with no loss of generality should ε be very small and μ be at least $O(1)$ as $\varepsilon \to 0$, we may consider the full system in the limit as $\varepsilon \to 0$ for our diffusive instability analysis since the root neglected by that quasi-equilibrium approximation is then highly stabilizing.

Recall from Table 1.2 that the ratios of the interaction dissipative rates and dispersal coefficients take on the values of $\varepsilon = 0.007$ and $\mu = 0.008$, respectively. Here, we have assigned the HIV infection dispersal coefficients of Stancevic *et al.* [24] to the corresponding ones for the EIAV infection. Our rationale in doing so is that the properties of these infections are similar enough for human disease virologists to refer to EIAV as the country cousin of HIV, which is explained in some depth by Cangelosi *et al.* [4]. Hence, not only is ε very small, but $\mu = O(\varepsilon)$ as well, more than justifying the employment of the quasi-equilibrium approximation on the unreduced ε-μ dependent model as asserted at the end of Section 1 which replaced its third governing partial
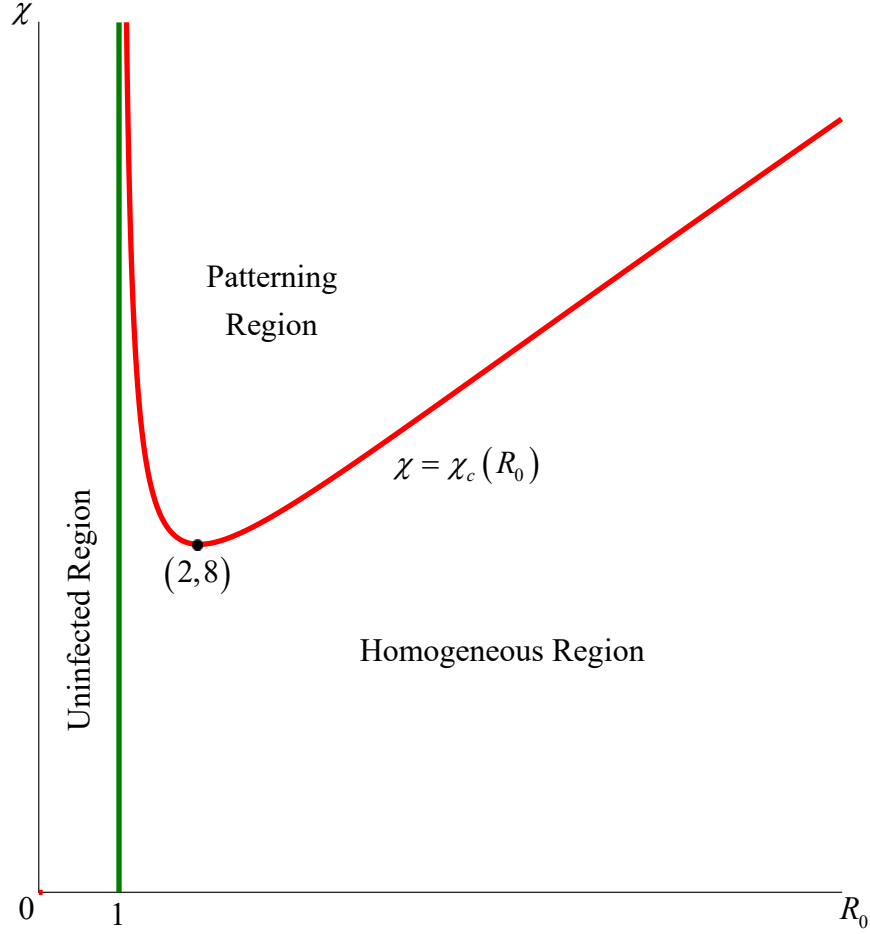
9

Figure 2.3: Plot in the R_0-χ plane summarizing our linear stability results designating the uninfected region which is characterized by $i_e \equiv 0$ for $0 < R_0 < 1$ and the marginal stability curve given by $\chi = \chi_c(R_0)$ for $R_0 > 1$, which has vertical asymptote $R_0 = 1$ and minimum point $(2, 8)$. The infected patterning region occurs when $\chi > \chi_c$ and the patterns in that region are the subject of our next three sections, while the infected homogeneous region occurs when $0 < \chi < \chi_c$ and is characterized by $i_e = 1 - 1/R_0 > 0$, which ranges from sparse, I$^-$ $(0 < i_e < 1/2$ for $1 < R_0 < 2)$, to dense, I$^+$ $(1/2 < i_e < 1$ for $R_0 > 2)$, as R_0 increases over its domain of definition $1 < R_0 < \infty$ for that component of the community equilibrium point. This marginal stability curve has been determined analytically in closed form, unlike the results of Stancevic *et al.* [24] obtained numerically which is the primary advantage of our adopting the quasi-equilibrium approximation.

differential equation (1.3c) by the algebraic relation $v = R_0 i$. Then substitution of this relation into its first two partial differential equations (1.3a,1.3b) yielded our quasi-equilibrium EIAV-target cell interaction-dispersion-chemotactic two-component model system (1.4) just analyzed for linear diffusive instabilities. As the caption of Fig. 2.3 indicates, patterns in its patterning region are the subject of Sections 3-5, the first two of which develop longitudinal and rhombic planform weakly

10

nonlinear stability analyses, respectively, of the infectious solution to this reduced model system, where its chemotactic term has been split into two parts by introducing the appropriate identity for the divergence of a scalar field times a gradient vector of

$$\boldsymbol{\nabla} \cdot (m\boldsymbol{\nabla} i) = \boldsymbol{\nabla} m \cdot \boldsymbol{\nabla} i + m\nabla^2 i. \tag{2.22}$$

3 Longitudinal Planform Nonlinear Stability Analysis

Consider a longitudinal planform solution to our quasi-equilibrium EIAV-target cell interaction-dispersion-chemotaxis model system for $m = m(x, y, t)$ and $i = i(x, y, t)$:

$$\frac{\partial m}{\partial t} = 1 - m - R_0 mi + \nabla^2 m - \chi(\boldsymbol{\nabla} m \cdot \boldsymbol{\nabla} i + m\nabla^2 i), \quad \frac{\partial i}{\partial t} = R_0 mi - i + \nabla^2 i; \tag{3.1a,b}$$

$$R_0 = \frac{\lambda\beta b}{\rho^2\gamma}, \ \chi = \frac{\lambda\chi_1}{\rho D_1}, \ \boldsymbol{\nabla} \equiv \left(\frac{\partial}{\partial x}, \frac{\partial}{\partial y}\right), \ \text{and } \nabla^2 = \boldsymbol{\nabla} \cdot \boldsymbol{\nabla}; \tag{3.1c}$$

of the form (Wollkind and Dichone, [30])

$$\begin{bmatrix} m \\ i \end{bmatrix}(x, y, t) \sim \begin{bmatrix} m_e \\ i_e \end{bmatrix} + A(t) \begin{bmatrix} m_{11} \\ i_{11} \end{bmatrix} \cos(q_c x) + A^2(t) \left\{ \begin{bmatrix} m_{20} \\ i_{20} \end{bmatrix} + \begin{bmatrix} m_{22} \\ i_{22} \end{bmatrix} \cos(2q_c x) \right\}$$

$$+ A^3(t) \left\{ \begin{bmatrix} m_{31} \\ i_{31} \end{bmatrix} \cos(q_c x) + \begin{bmatrix} m_{33} \\ i_{33} \end{bmatrix} \cos(3q_c x) \right\} \tag{3.2a}$$

where $m_e = 1/R_0$, $i_e = (R_0 - 1)/R_0 > 0$, $q_c^2 = q_c^2(R_0) = \sqrt{R_0 - 1}$, and the amplitude function $A(t)$ satisfies the Landau [14] equation

$$\frac{dA}{dt} \sim \sigma_0 A - a_1 A^3. \tag{3.2b}$$

Here $\sigma_0 = \sigma_0(\chi; R_0)$ is that root of the quadratic secular equation

$$f(\sigma; q_c^2) = \sigma^2 + (2q_c^2 + R_0)\sigma + (R_0 + q_c^2)q_c^2 + (R_0 - 1)\left(1 - \frac{\chi q_c^2}{R_0}\right) = 0 \tag{3.3a}$$

satisfying

$$2\sigma_0 = -(2q_c^2 + R_0) + \sqrt{(2q_c^2 + R_0)^2 + 4(R_0 - 1)\left(\frac{q_c^2}{R_0}\right)(\chi - \chi_c)} \tag{3.3b}$$

where

$$\chi_c = \chi_c(R_0) = \frac{R_0}{R_0 - 1}\left(R_0 + q_c^2 + \frac{R_0 - 1}{q_c^2}\right) = \frac{R_0^2}{R_0 - 1} + 2\frac{R_0}{\sqrt{R_0 - 1}}, \tag{3.3c}$$

such that $\sigma_0(\chi_c; R_0) = 0$, $\sigma_0(\chi; R_0) > 0$ for $\chi > \chi_c$, and $\text{Re}[\sigma_0(\chi; R_0)] < 0$ for $\chi < \chi_c$, while we shall take χ sufficient close to χ_c so that σ_0 is still real when $0 < \chi < \chi_c$, in which case this last inequality reduces to $\sigma_0(\chi; R_0) < 0$. Finally, the notation m_{jn} and i_{jn} is being employed for the coefficients in each term in the above expansion proportional to $A^j(t)\cos(nq_c x)$.

Then substituting this solution into our basic system (3.1), employing the relevant trigonometric identities for the products of the cosine functions in mi and $m\nabla^2 i$ and of the sine functions in

11

$\boldsymbol{\nabla} m \cdot \boldsymbol{\nabla} i$, and making use of the Landau amplitude equation, yields the following problems, one proportional to each term appearing in that solution:

$A(t)\cos(q_c x)$:

$$(\sigma_0 + R_0 + q_c^2)m_{11} + \left(1 - \frac{\chi q_c^2}{R_0}\right)i_{11} = 0, \tag{3.4a}$$

$$-(R_0 - 1)m_{11} + (\sigma_0 + q_c^2)i_{11} = 0. \tag{3.4b}$$

Note that this is equivalent to our linear stability problem for the community equilibrium point evaluated at $q^2 = q_c^2$ and $\sigma = \sigma_0$. Hence we can conclude that its determinant $f(\sigma_0; q_c^2) = 0$. Thus we may assign the value $i_{11} = 1$ which then implies that $m_{11} = (\sigma_0 + q_c^2)/(R_0 - 1)$ and, when $\chi = \chi_c$, the latter becomes $[m_{11}]_{\chi=\chi_c} = q_c^2/(R_0 - 1)$.

There are two second order problems given by:

$A^2(t)$:

$$(2\sigma_0 + R_0)m_{20} + i_{20} = -\frac{R_0 m_{11} i_{11}}{2}, \tag{3.5a}$$

$$-(R_0 - 1)m_{20} + 2\sigma_0 i_{20} = \frac{R_0 m_{11} i_{11}}{2}. \tag{3.5b}$$

$A^2(t)\cos(2q_c x)$:

$$(2\sigma_0 + R_0 + 4q_c^2)m_{22} + \left(1 - \frac{4\chi q_c^2}{R_0}\right)i_{22} = \frac{(-R_0 + 2\chi q_c^2)m_{11} i_{11}}{2}, \tag{3.6a}$$

$$-(R_0 - 1)m_{22} + (2\sigma_0 + 4q_c^2)i_{22} = \frac{R_0 m_{11} i_{11}}{2}. \tag{3.6b}$$

These problems can be solved in a straightforward manner to yield:

$$m_{20} = \begin{vmatrix} -1 & 1 \\ 1 & 2\sigma_0 \end{vmatrix} \frac{R_0 m_{11} i_{11}}{2f(2\sigma_0; 0)}, \tag{3.7a}$$

$$i_{20} = \begin{vmatrix} 2\sigma_0 + R_0 & -1 \\ 1 - R_0 & 1 \end{vmatrix} \frac{R_0 m_{11} i_{11}}{2f(2\sigma_0; 0)}; \tag{3.7b}$$

$$m_{22} = \begin{vmatrix} -R_0 + 2\chi q_c^2 & 1 - \frac{4\chi q_c^2}{R_0} \\ R_0 & 2\sigma_0 + 4q_c^2 \end{vmatrix} \frac{m_{11} i_{11}}{2f(2\sigma_0; 4q_c^2)}, \tag{3.8a}$$

$$i_{22} = \begin{vmatrix} 2\sigma_0 + R_0 + 4q_c^2 & -R_0 + 2\chi q_c^2 \\ -(R_0 - 1) & R_0 \end{vmatrix} \frac{m_{11} i_{11}}{2f(2\sigma_0; 4q_c^2)}; \tag{3.8b}$$

which, when $\chi = \chi_c$, become:

$$[i_{20}]_{\chi=\chi_c} = -[m_{20}]_{\chi=\chi_c} = R_0[m_{11}]_{\chi=\chi_c} \frac{i_{11}}{2(R_0 - 1)}; \tag{3.9a}$$

$$[m_{22}]_{\chi=\chi_c} = \{4q_c^2[-R_0 + \chi_c(2q_c^2 + 1)] - R_0\}[m_{11}]_{\chi=\chi_c} \frac{i_{11}}{18(R_0 - 1)}, \tag{3.9b}$$

12

$$[i_{22}]_{\chi=\chi_c} = \{R_0 + 2q_c^2[2R_0 + \chi_c(R_0 - 1)]\}[m_{11}]_{\chi=\chi_c}\frac{i_{11}}{18(R_0 - 1)}. \tag{3.9c}$$

Although there are also two third order problems, we need only consider the one proportional to $\cos(q_c x)$ which contains the Landau coefficient a_1 for our Fredholm method of solvability:

$A^3(t)\cos(q_c x)$:

$$(3\sigma_0 + R_0 + q_c^2)m_{31} + \left(1 - \frac{\chi q_c^2}{R_0}\right)i_{31} = a_1 m_{11} + r_{31}^{(1)} \tag{3.10a}$$

where

$$r_{31}^{(1)} = \chi q_c^2\left[\left(m_{20} - \frac{m_{22}}{2}\right)i_{11} + m_{11}i_{22}\right] - r_{31}^{(2)} \tag{3.10b}$$

and

$$-(R_0 - 1)m_{31} + (3\sigma_0 + q_c^2)i_{31} = a_1 i_{11} + r_{31}^{(2)} \tag{3.11a}$$

where

$$r_{31}^{(2)} = R_0\left[m_{11}\left(i_{20} + \frac{i_{22}}{2}\right) + \left(m_{20} + \frac{m_{22}}{2}\right)i_{11}\right]. \tag{3.11b}$$

Defining the vectors

$$\mathbf{v}_{jk} = \begin{bmatrix} m_{jk} \\ i_{jk} \end{bmatrix}, \quad \mathbf{v}_{11}^+ = \begin{bmatrix} m_{11}^+ \\ i_{11}^+ \end{bmatrix}, \quad \mathbf{r}_{31} = \begin{bmatrix} r_{31}^{(1)} \\ r_{31}^{(2)} \end{bmatrix}; \tag{3.12a}$$

and matrices

$$M = \begin{pmatrix} R_0 + q_c^2 & 1 - \frac{\chi q_c^2}{R_0} \\ -(R_0 - 1) & q_c^2 \end{pmatrix}, \quad M^+ = M^T = \begin{pmatrix} R_0 + q_c^2 & -(R_0 - 1) \\ 1 - \frac{\chi q_c^2}{R_0} & q_c^2 \end{pmatrix}; \tag{3.12b}$$

this system can be represented in vector form as

$$3\sigma_0\mathbf{v}_{31} + M\mathbf{v}_{31} = a_1\mathbf{v}_{11} + \mathbf{r}_{31}. \tag{3.13}$$

Defining the inner product for the vectors $\mathbf{u} = \begin{bmatrix} u_1 \\ u_2 \end{bmatrix}$ and $\mathbf{v} = \begin{bmatrix} v_1 \\ v_2 \end{bmatrix}$ by

$$\mathbf{u} \cdot \mathbf{v} = u_1 v_1 + u_2 v_2; \tag{3.14}$$

and taking the inner product of (3.13) with $\mathbf{v}_{11}^+$ where

$$(\sigma_0 J + M^T)\mathbf{v}_{11}^+ = \mathbf{0} = \begin{bmatrix} 0 \\ 0 \end{bmatrix} \text{ with } J = \begin{pmatrix} 1 & 0 \\ 0 & 1 \end{pmatrix} \text{ and } \det(\sigma_0 J + M^T) = f(\sigma_0; q_c^2) = 0; \tag{3.15}$$

we obtain

$$3\sigma_0\mathbf{v}_{31} \cdot \mathbf{v}_{11}^+ + M\mathbf{v}_{31} \cdot \mathbf{v}_{11}^+ = a_1\mathbf{v}_{11} \cdot \mathbf{v}_{11}^+ + \mathbf{r}_{31} \cdot \mathbf{v}_{11}^+. \tag{3.16}$$

Then, since

$$M\mathbf{v}_{31} \cdot \mathbf{v}_{11}^+ = \mathbf{v}_{31} \cdot M^+\mathbf{v}_{11}^+ = \mathbf{v}_{31} \cdot M^T\mathbf{v}_{11}^+ \text{ and } M^T\mathbf{v}_{11}^+ = -\sigma_0\mathbf{v}_{11}^+, \tag{3.17a}$$

we can conclude that

$$M\mathbf{v}_{31} \cdot \mathbf{v}_{11}^+ = -\sigma_0\mathbf{v}_{31} \cdot \mathbf{v}_{11}^+. \tag{3.17b}$$

13

Hence (3.16) becomes

$$2\sigma_0 \mathbf{v}_{31} \cdot \mathbf{v}_{11}^+ = a_1 \mathbf{v}_{11} \cdot \mathbf{v}_{11}^+ + \mathbf{r}_{31} \cdot \mathbf{v}_{11}^+. \tag{3.17c}$$

Now noting that

$$(\sigma_0 + R_0 + q_c^2)m_{11}^+ = (R_0 - 1)i_{11}^+, \tag{3.18a}$$

we assign the value $m_{11}^+ = 1$ which then implies that $i_{11}^+ = (\sigma_0 + R_0 + q_c^2)/(R_0 - 1)$. Thus,

$$\mathbf{v}_{11} \cdot \mathbf{v}_{11}^+ = m_{11} + i_{11}^+ = \frac{2\sigma_0 + R_0 + 2q_c^2}{R_0 - 1}. \tag{3.18b}$$

Finally taking the limit of (3.17c) as $\chi \to \chi_c$ and recalling that $\sigma_0(\chi_c; R_0) = 0$, we obtain the solvability condition

$$a_1 = a_1(R_0) = \frac{-1}{2q_c^2 + R_0} \left[(R_0 - 1)r_{31}^{(1)} + (q_c^2 + R_0)r_{31}^{(2)} \right]_{\chi=\chi_c}. \tag{3.19}$$

As a check on this adjoint operator method of calculating a_1, we now use a direct method of computation. Eliminating m_{31} by solving the $A^3(t)\cos(q_c x)$ equations (3.10a) and (3.11a) simultaneously and then employing our choice for the components of $\mathbf{v}_{11}$, as well as the secular equation, we find that i_{31} and a_1 satisfy the relation

$$2\sigma_0 i_{31} - a_1 = \frac{(R_0 - 1)r_{31}^{(1)} + (3\sigma_0 + R_0 + q_c^2)r_{31}^{(2)}}{4\sigma_0 + 2q_c^2 + R_0}. \tag{3.20a}$$

Now taking the limit of (3.20a) as $\chi \to \chi_c$, assuming that i_{31} remains bounded in this limit (observe the adjoint operator method implicitly assumed a similar behavior for $\mathbf{v}_{31} \cdot \mathbf{v}_{11}^+$), and again recalling that $\sigma_0(\chi_c; R_0) = 0$, we obtain

$$a_1 = a_1(R_0) = \frac{-1}{2q_c^2 + R_0} \left[(R_0 - 1)r_{31}^{(1)} + (R_0 + q_c^2)r_{31}^{(2)} \right]_{\chi=\chi_c}, \tag{3.20b}$$

which, being equal to our solvability condition (3.19), serves as a partial check on that indirect adjoint operator method of derivation.

As described in Wollkind and Dichone [31], the stability behavior of the Landau equation truncated through terms of third-order and thus the pattern formation aspect of our model system is crucially dependent upon the sign of a_1. Hence, in order to determine that behavior, we examine this formula for a_1. Towards that end, we plot $a_1(R_0)$ versus R_0 in Fig. 3.1. From this figure, we observe that a_1 has a zero at $R_0 = R_c$ such that

$$a_1(R_0) < 0 \text{ for } 1 < R_0 < R_c, \ a_1(R_c) = 0, \ a_1(R_0) > 0 \text{ for } R > R_c; \tag{3.21a}$$

where

$$R_c = 1.761. \tag{3.21b}$$

Given the conditions for $\sigma_0(\chi; R_0)$ and $a_1(R_0)$ summarized in Figs. 2.3 and 3.1, respectively, we note that the Landau amplitude function $A(t)$ undergoes a pitchfork bifurcation (Walgraef, [28]) at $\chi = \chi_c(R_0)$, when $R_0 > R_c$ from which we can conclude that:
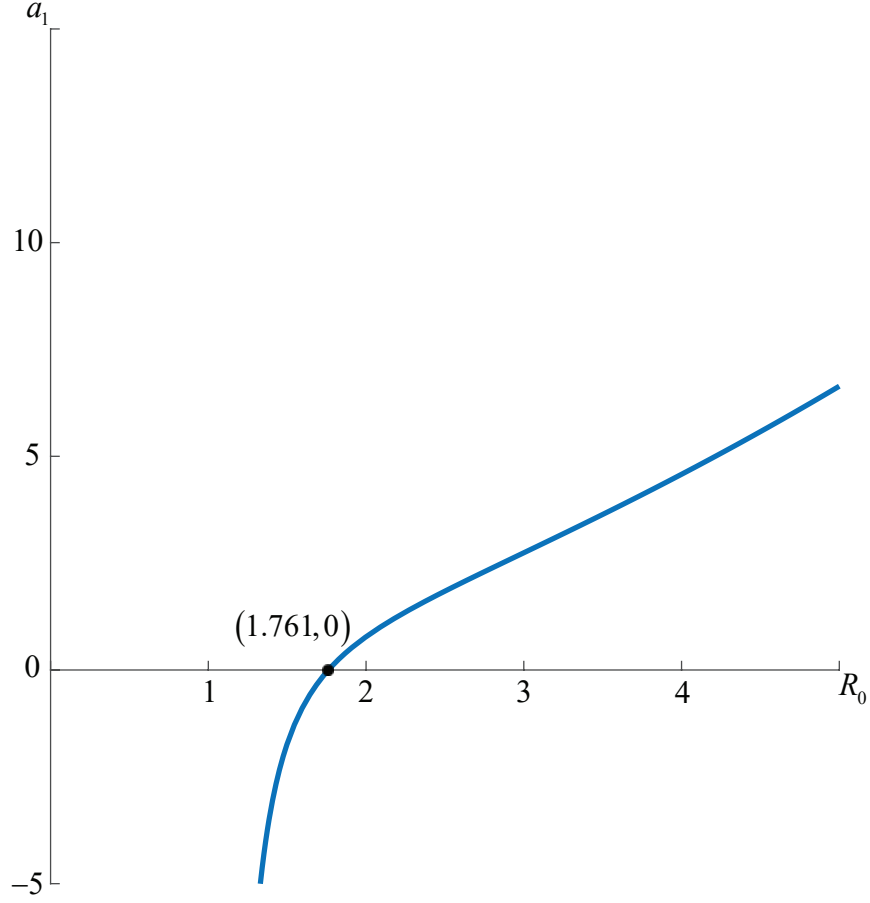
14

Figure 3.1: A plot of the longitudinal Landau coefficient $a_1(R_0)$ versus R_0. Note that $a_1(R_c) = 0$ for $R_c = 1.761$, $a_1(R_0) < 0$ for $1 < R_0 < R_c$, and $a_1(R_0) > 0$ for $R_c < R_0 < \infty$.

- For $0 < \chi < \chi_c(R_0)$ and $R_0 > R_c$, the undisturbed state $A = 0$ is stable since $\sigma_0 < 0$ and $a_1 > 0$, yielding a uniform homogeneous distribution $i(x, y, t) \to i_e(R_0) = 1 - 1/R_0$ as $t \to \infty$.

- For $\chi > \chi_c(R_0)$ and $R_0 > R_c$, $A = A_e = \sqrt{\sigma_0/a_1}$ is stable since $\sigma_0, a_1 > 0$, yielding a periodic one-dimensional pattern consisting of stationary parallel stripes

$$i(x, y, t) \to i_e(R_0) + A_e \cos\left(\frac{2\pi x}{\lambda_c}\right) \text{ as } t \to \infty \qquad (3.22\text{a})$$

with characteristic wavelength of

$$\lambda_c = \frac{2\pi}{q_c}. \qquad (3.22\text{b})$$

These supercritical stripes are represented in the contour plot of Fig. 3.2 where regions of elevated target cell infectivity $(i > i_e)$ appear red and those of depressed infectivity $(i < i_e)$, white. Here,
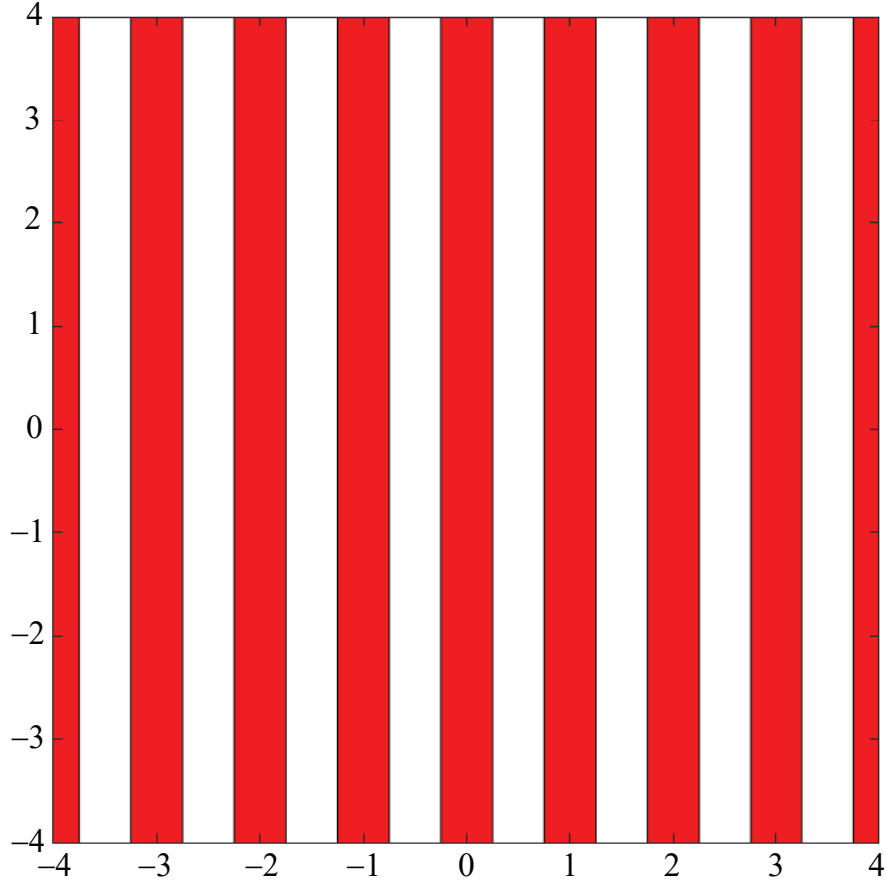
15

Figure 3.2: Contour plot in the x-y plane for supercritical stripes (critical point II of the rhombic planform nonlinear stability analysis of Section 4) where the spatial variables are measured in units of λ_c. Here, regions of elevated infectivity $(i > i_e)$ appear red and ones of depressed infectivity $(i < i_e)$, white. This transition occurs at $i = i_e$, which is a protocol that will be labeled zero threshold for our rhombic planform nonlinear stability analysis. We shall show in Section 5 that critical point II can not occur here, but if it did only patterns of zero threshold could be produced.

the axes are being measured in units of λ_c. We wish to offer an interpretation of a_1 becoming large as $R_0 > R_c$ increases (see Fig. 3.1). Then $\sigma_0/a_1 = \varepsilon_0^2$ must be small for $\chi > \chi_c$ reasonably far from the marginal stability curve. Thus, dividing the truncated Landau equation by a_1 and introducing the rescaled time and amplitude $t_1 = \sigma_0 t$ and $A_1(t_1) = A(t)/\varepsilon_0$, we would, as usual, obtain the transformed Landau equation $dA_1/dt_1 \sim A_1 - A_1^3$, which justifies that expansion procedure in this supercritical regime. When $1 < R_0 < R_c$, that bifurcation is subcritical. The consequences of such subcritical behavior will be discussed in Section 5.

As was true for our linear stability analysis of Section 2, this longitudinal planform nonlinear stability analysis has been restricted to one-dimensional disturbances. In the next section, after

Sekimura *et al.*'s [23] study of butterfly wing patterning (Nijhout, [18]), we shall investigate the possibility of occurrence of the two-dimensional petechial hemorrhage-type patterns described in Section 1 by performing a rhombic planform nonlinear stability analysis of the infectious state for our quasi-equilibrium EIAV-target cell interaction-dispersion-chemotaxis model system (3.1) in its supercritical regime, where $R_0 > R_c$. The one-dimensional disturbances considered in this section are a special case of those two-dimensional disturbances characteristic of that rhombic planform nonlinear stability analysis. Although finding these quantities just calculated is a necessary precondition for the completion of that method, they are found more easily by this sequential process rather than solving for them all in the rhombic planform analysis.

In performing that rhombic planform analysis, we shall be closely following the approach of Chaiya *et al.* [6] whose vegetative rhombic pattern formation for their interaction-diffusion plant-ground water model system in an arid flat environment was driven by root suction which acted as a plant cross-diffusive effect in their ground water governing equation. As in our Sections 2 and 3, they first completed linear diffusive instability analyses of their bare ground and community equilibrium points and a longitudinal planform nonlinear stability analysis of the latter before finally performing a rhombic planform nonlinear stability analysis of this community equilibrium state to determine the Turing diffusive instability behavior of that system. Their theoretical results were plotted in a rainfall-root suction space with a characteristic curve as a function of saturation along which a standard morphological vegetative sequence was predicted.

4 Rhombic Planform Nonlinear Stability Analysis

Consider a rhombic planform solution to our quasi-equilibrium EIAV-target cell interaction-dispersion-chemotaxis model system (3.1) for $m = m(x, y, t)$ and $i = i(x, y, t)$ of the form (Wollkind and Dichone, [30]):

$$
\begin{bmatrix} m \\ i \end{bmatrix}(x,y,t) \sim \begin{bmatrix} m_e \\ i_e \end{bmatrix} + A(t)\begin{bmatrix} m_{1010} \\ i_{1010} \end{bmatrix}\cos(q_c x) + B(t)\begin{bmatrix} m_{0101} \\ i_{0101} \end{bmatrix}\cos(q_c z)
$$

$$
+ A^2(t)\left\{ \begin{bmatrix} m_{2000} \\ i_{2000} \end{bmatrix} + \begin{bmatrix} m_{2020} \\ i_{2020} \end{bmatrix}\cos(q_c x) \right\}
$$

$$
+ A(t)B(t)\left\{ \begin{bmatrix} m_{1111} \\ i_{1111} \end{bmatrix}\cos(q_c\{x+z\}) + \begin{bmatrix} m_{111(-1)} \\ i_{111(-1)} \end{bmatrix}\cos(q_c\{x-z\}) \right\}
$$

$$
+ B^2(t)\left\{ \begin{bmatrix} m_{0200} \\ i_{0200} \end{bmatrix} + \begin{bmatrix} m_{0202} \\ i_{0202} \end{bmatrix}\cos(2q_c z) \right\}
$$

$$
+ A^3(t)\left\{ \begin{bmatrix} m_{3010} \\ i_{3010} \end{bmatrix}\cos(q_c x) + \begin{bmatrix} m_{3030} \\ i_{3030} \end{bmatrix}\cos(3q_c x) \right\}
$$

$$
+ A^2(t)B(t)\left\{ \begin{bmatrix} m_{2101} \\ i_{2101} \end{bmatrix}\cos(q_c z) + \begin{bmatrix} m_{2121} \\ i_{2121} \end{bmatrix}\cos(q_c\{2x+z\}) + \begin{bmatrix} m_{212(-1)} \\ i_{212(-1)} \end{bmatrix}\cos(q_c\{2x-z\}) \right\}
$$

$$
+ A(t)B^2(t)\left\{ \begin{bmatrix} m_{1210} \\ i_{1210} \end{bmatrix}\cos(q_c x) + \begin{bmatrix} m_{1212} \\ i_{1212} \end{bmatrix}\cos(q_c\{x+2z\}) + \begin{bmatrix} m_{121(-2)} \\ i_{121(-2)} \end{bmatrix}\cos(q_c\{x-2z\}) \right\}
$$

$$
+ B^3(t)\left\{ \begin{bmatrix} m_{0301} \\ i_{0301} \end{bmatrix}\cos(q_c z) + \begin{bmatrix} m_{0303} \\ i_{0303} \end{bmatrix}\cos(3q_c z) \right\}, \quad (4.1a)
$$

where $m_e = 1/R_0$, $i_e = (R_0 - 1)/R_0$; $q_c^2 = q_c^2(R_0) = \sqrt{R_0 - 1}$; $z = x\cos(\varphi) + y\sin(\varphi)$ with $\varphi \in (0, \pi/2] \equiv$ the rhombic angle; and the amplitude functions $A(t)$ and $B(t)$ satisfy the Landau equations

$$\frac{dA}{dt} \sim \sigma A - A(a_1 A^2 + b_1 B^2) = F(A, B), \tag{4.1b}$$

$$\frac{dB}{dt} \sim \sigma B - B(b_1 A^2 + a_1 B^2) = G(A, B). \tag{4.1c}$$

Here the notation $m_{j\ell nk}$ and $i_{j\ell nk}$ is being employed for the coefficients of each term in the above expansion proportional to $A^j(t)B^\ell(t)\cos(q_c\{nx + kz\})$.

Then substituting this solution into our basic system (3.1), employing the relevant trigonometric identities for the products of the cosine functions in mi and $m\nabla^2 i$ and of the sine functions in $\nabla m \cdot \nabla i$, and making use of the Landau amplitude equations, yields the following solutions:

$$\sigma = \sigma_0(\chi; R_0), \ m_{j0n0} = m_{0j0n} = m_{jn}(\chi; R_0), \ i_{j0n0} = i_{0j0n} = i_{jn}(\chi; R_0), \ a_1 = a_1(R_0); \tag{4.2}$$

and the particular problems proportional to $A(t)B(t)\cos(q_c[x \pm z])$ and $A^2(t)B(t)\cos(q_c z)$:

$A(t)B(t)\cos(q_c[x \pm z])$:

$$(2\sigma_0 + R_0 + 2[1 \pm \cos(\varphi)]q_c^2)m_{111(\pm 1)} + \left(1 - 2[1 \pm \cos(\varphi)]\frac{\chi q_c^2}{R_0}\right)i_{111(\pm 1)}$$
$$= (-R_0 + [1 \pm \cos(\varphi)]\chi q_c^2)m_{11}i_{11}, \tag{4.3a}$$

$$-(R_0 - 1)m_{111(\pm 1)} + (2\sigma_0 + 2[1 \pm \cos(\varphi)]q_c^2)i_{111(\pm 1)} = R_0 m_{11}i_{11}. \tag{4.3b}$$

$A^2(t)B(t)\cos(q_c z)$:

$$(3\sigma_0 + R_0 + q_c^2)m_{2101} + \left(1 - \frac{\chi q_c^2}{R_0}\right)i_{2101} = b_1 m_{11} + r_{2101}^{(1)} \tag{4.4a}$$

where

$$r_{2101}^{(1)} = \chi q_c^2 \left(m_{11}\frac{[1 + \cos(\varphi)]i_{1111} + [1 - \cos(\varphi)]i_{111(-1)}}{2}\right.$$
$$\left. + \left[m_{20} + \cos(\varphi)\frac{m_{111(-1)} - m_{1111}}{2}\right]i_{11}\right) - r_{2101}^{(2)} \tag{4.4b}$$

and

$$-(R_0 - 1)m_{2101} + (3\sigma_0 + q_c^2)i_{2101} = b_1 i_{11} + r_{2101}^{(2)} \tag{4.5a}$$

where

$$r_{2101}^{(2)} = R_0 \left(m_{11}\left[i_{20} + \frac{i_{1111} + i_{111(-1)}}{2}\right] + \left[m_{20} + \frac{m_{1111} + m_{111(-1)}}{2}\right]i_{11}\right). \tag{4.5b}$$

18

Using the notation of our longitudinal planform analysis, the second-order systems can be solved in a straightforward manner to yield

$$
m_{111(\pm 1)} = \frac{\begin{vmatrix} -R_0 + [1 \pm \cos(\varphi)]\chi q_c^2 & 1 - 2[1 \pm \cos(\varphi)]\frac{\chi q_c^2}{R_0} \\ R_0 & 2\sigma_0 + 2[1 \pm \cos(\varphi)]q_c^2 \end{vmatrix} m_{11} i_{11}}{f(2\sigma_0; 2[1 \pm \cos(\varphi)]q_c^2)},
$$

$$
i_{111(\pm 1)} = \frac{\begin{vmatrix} 2\sigma_0 + R_0 + 2[1 \pm \cos(\varphi)]q_c^2 & -R_0 + [1 \pm \cos(\varphi)]\chi q_c^2 \\ -(R_0 - 1) & R_0 \end{vmatrix} m_{11} i_{11}}{f(2\sigma_0; 2[1 \pm \cos(\varphi)]q_c^2)};
$$

(4.6a)

which, when $\chi = \chi_c$, become:

$$
[m_{111(\pm 1)}]_{\chi = \chi_c} = \frac{2[1 \pm \cos(\varphi)]q_c^2\{-R_0 + \chi_c([1 \pm \cos(\varphi)]q_c^2 + 1)\} - R_0}{(2[1 \pm \cos(\varphi)] - 1)^2(R_0 - 1)}[m_{11}]_{\chi = \chi_c} i_{11},
$$

$$
[i_{111(\pm 1)}]_{\chi = \chi_c} = \frac{R_0 + [1 \pm \cos(\varphi)]q_c^2[2R_0 + \chi_c(R_0 - 1)]}{(2[1 \pm \cos(\varphi)] - 1)^2(R_0 - 1)}[m_{11}]_{\chi = \chi_c} i_{11};
$$

(4.6b)

while the third-order system may be represented in the vector form

$$
3\sigma_0 \mathbf{v}_{2101} + M\mathbf{v}_{2101} = b_1 \mathbf{v}_{11} + \mathbf{r}_{2101} \tag{4.7a}
$$

where

$$
\mathbf{v}_{2101} = \begin{bmatrix} m_{2101} \\ i_{2101} \end{bmatrix} \text{ and } \mathbf{r}_{2101} = \begin{bmatrix} r_{2101}^{(1)} \\ r_{2101}^{(2)} \end{bmatrix}. \tag{4.7b}
$$

Now taking the inner product of (4.7a) with $\mathbf{v}_{11}^+$ and deducing in a similar manner to (3.17b) that

$$
M\mathbf{v}_{2101} \cdot \mathbf{v}_{11}^+ = -\sigma_0 \mathbf{v}_{2101} \cdot \mathbf{v}_{11}^+, \tag{4.8a}
$$

we obtain the scalar relation

$$
2\sigma_0 \mathbf{v}_{2101} \cdot \mathbf{v}_{11}^+ = b_1 \mathbf{v}_{11} \cdot \mathbf{v}_{11}^+ + \mathbf{r}_{2101} \cdot \mathbf{v}_{11}^+. \tag{4.8b}
$$

Further, recalling that

$$
m_{11} = \frac{\sigma_0 + q_c^2}{R_0 - 1}, \quad i_{11} = 1, \quad m_{11}^+ = 1, \quad i_{11}^+ = \frac{\sigma_0 + R_0 + q_c^2}{R_0 - 1}, \tag{4.9a}
$$

we reproduce (3.18b)

$$
\mathbf{v}_{11} \cdot \mathbf{v}_{11}^+ = m_{11} + i_{11}^+ = \frac{2\sigma_0 + R_0 + 2q_c^2}{R_0 - 1}. \tag{4.9b}
$$

Finally employing these results of (4.9) in (4.8b) and taking its limit as $\chi \to \chi_c$, we obtain the solvability condition for our rhombic Landau coefficient

$$
b_1 = b_1(R_0, \varphi) = \frac{-1}{2q_c^2 + R_0}[(R_0 - 1)r_{2101}^{(1)} + (q_c^2 + R_0)r_{2101}^{(2)}]_{\chi = \chi_c}, \tag{4.10}
$$

since $\sigma_0(\chi_c; R_0) = 0$.

Having developed these formulae for its growth rate and Landau coefficients, we turn our attention to the rhombic planform amplitude equations which possess the following equivalence classes of critical points (A_0, B_0) such that $F(A_0, B_0) = G(A_0, B_0) = 0$ with $A_0, B_0 \geq 0$ given by

$$\text{I: } A_0 = B_0 = 0; \quad \text{II: } A_0^2 = \frac{\sigma_0}{a_1}, \ B_0 = 0; \quad \text{V: } A_0 = B_0 \text{ with } A_0^2 = \frac{\sigma_0}{a_1 + b_1}. \tag{4.11}$$

Here, $a_1 > 0$, since we are considering $R_0 > R_c$ and further assume that $a_1 + b_1 > 0$ as well. Hence, critical points II and V would only occur provided $\sigma_0 > 0$ or $\chi > \chi_c$.

We first perform a linear stability analysis of these critical points by seeking a solution of our rhombic planform amplitude equations of the form

$$A(t) = A_0 + \varepsilon_1 \mathscr{A}(t) + O(\varepsilon_1^2), \ B(t) = B_0 + \varepsilon_1 \mathscr{B}(t) + O(\varepsilon_1^2) \text{ with } |\varepsilon_1| \ll 1; \tag{4.12}$$

expanding the functions F, G in Taylor series about $A = A_0$, $B = B_0$; neglecting terms of $O(\varepsilon_1^2)$; and cancelling the resultant common ε_1 factor; to determine that the perturbation quantities $\mathscr{A}(t), \mathscr{B}(t)$ satisfy the following linear homogeneous ordinary differential equation system:

$$\frac{d\mathscr{A}}{dt} = c_{11}\mathscr{A} + c_{12}\mathscr{B}, \quad \frac{d\mathscr{B}}{dt} = c_{21}\mathscr{A} + c_{22}\mathscr{B}, \tag{4.13a}$$

where

$$\begin{aligned}
c_{11} &= \frac{\partial F}{\partial A}(A_0, B_0) = \sigma_0 - 3a_1 A_0^2 - b_1 B_0^2, \\
c_{22} &= \frac{\partial G}{\partial B}(A_0, B_0) = \sigma_0 - 3a_1 B_0^2 - b_1 A_0^2, \\
c_{12} &= \frac{\partial F}{\partial B}(A_0, B_0) = c_{21} = \frac{\partial G}{\partial A}(A_0, B_0) = -2b_1 A_0 B_0.
\end{aligned} \tag{4.13b}$$

Then, letting $[\mathscr{A}, \mathscr{B}](t) = [C_1, C_2]e^{pt}$, where $|C_1|^2 + |C_2|^2 \neq 0$, we obtain the following linear homogeneous system for the constants C_1 and C_2:

$$(p - c_{11})C_1 - c_{12}C_2 = 0, \ -c_{21}C_1 + (p - c_{22})C_2 = 0; \tag{4.14a}$$

which, upon imposition of the vanishing of the determinant of the matrix of its coefficients to guarantee the nontriviality property for these constants, yields the following quadratic in p:

$$(p - c_{11})(p - c_{22}) - c_{12}^2 = 0. \tag{4.14b}$$

Next, particularizing this quadratic to the specific (A_0, B_0) values of the critical points and noting that under these conditions it has the associated roots $p_1 = c_{11} + c_{12}$ and $p_2 = c_{22} - c_{12}$ since either $c_{12} = 0$ for I and II or $c_{11} = c_{22}$ for V, we conclude that

$$\text{I: } p_{1,2} = \sigma_0, \ \text{II: } p_1 = -2\sigma_0, \ p_2 = \frac{(a_1 - b_1)\sigma_0}{a_1}; \ \text{V: } p_1 = -2\sigma_0, \ p_2 = \frac{2(b_1 - a_1)\sigma_0}{a_1 + b_1}. \tag{4.15}$$

Finally, requiring $p_{1,2} < 0$, we deduce the stability criteria:

I is stable for $\sigma_0 < 0$; II is stable for $\sigma_0 > 0$, $b_1 > a_1$; V is stable for $\sigma_0 > 0$, $a_1 > b_1$. (4.16)

Observe that since those criteria are mutually exclusive there can never be pair-wise bistability between these critical points. Also note that $\sigma_0 > 0$ is both an existence condition and a stability criterion for critical points II and V.

Before examining the implications of those stability criteria, we make a morphological interpretation of the potentially stable critical points relative to the infectivity patterns under investigation. Then, to lowest order, the long-time behavior of the i-density deviation from equilibrium associated with these critical points is given by $\lim_{t\to\infty}[i(x,y,t) - i_e] \sim \Delta i_e(x,y)$, where

$$\Delta i_e(x,y) = A_0 \cos(q_c x) + B_0 \cos(q_c z) \text{ for } z = x\cos(\varphi) + y\sin(\varphi). \tag{4.17}$$

Thus critical points I and II correspond to the homogeneous distributions and parallel stripes, respectively, already discussed in the longitudinal analysis. To make an analogous interpretation of critical point V, we consider this deviation function with $A_0 = B_0 > 0$ and introduce the concept of higher, zero, and lower threshold patterns based upon the mean density deviation level of the infected target cells. To do so, we must first examine what, in fluid mechanics, are called the mean motion terms (Segel, [22]) that our nonlinear stability analysis has induced on that density level. These homogeneous higher-order terms in $\lim_{t\to\infty}[i(x,y,t) - i_e]$ for critical point V are given by

$$i_{2000}A_0^2 + i_{0200}B_0^2 \text{ with } A_0 = B_0 \text{ or } 2i_{20}B_0^2 \text{ since } i_{0200} = i_{2000} = i_{20}. \tag{4.18a}$$

Then, adding these terms to the original zero mean level of that density deviation, we find that this mean level to second-order now satisfies

$$\Delta i_m = 2i_{20}B_0^2. \tag{4.18b}$$

We next adopt the protocol (Wollkind and Dichone, [31]) that in our contour plots related to critical point V the elevations, which satisfy $\Delta i_e > \Delta i_m$, appear red, and depressions, which satisfy $\Delta i_e < \Delta i_m$, white, where the threshold value at which this transition occurs is given by $\Delta i_e = \Delta i_m$. When i_{20} is greater than, equal to, or less than zero we label such patterns as being of higher, zero, or lower threshold, respectively. Hence, to determine the proper threshold type we have to examine the sign of i_{20}, which will be done at the beginning of Section 5. To make a physical interpretation of these results, we note that to lowest order the equilibrium i-density deviation pattern associated with critical point V satisfies

$$\Delta i_e(x,y) = B_0 \left[\cos\left(\frac{2\pi x}{\lambda_c}\right) + \cos\left(\frac{2\pi z}{\lambda_c}\right) \right] = B_0 g(x,z) \tag{4.19a}$$

$$\text{for } z = x\cos(\varphi) + y\sin(\varphi). \tag{4.19b}$$

The three parts of Fig. 4.1 are threshold contour plots of $g(x,z)$ for the typical rhombic angle (see below) $\varphi = 0.625$ with the threshold values of 1, 0, and -1, respectively. Here, the spatial variables are being measured in units of λ_c with regions exceeding that threshold in each part appearing red and regions below it, white. Given their appearance in Fig. 4.1 we associate these higher, zero, and lower threshold-type rhombic arrays with infection patterns of spots, rectangles, and gaps, respectively, denoting them by V^+, V^0, and V^- in that figure and in the next section.

21

$$\varphi = 0.625\ (36°)$$

$\mathrm{V^+}$: Spots $\mathrm{V^0}$: Rectangles $\mathrm{V^-}$: Gaps
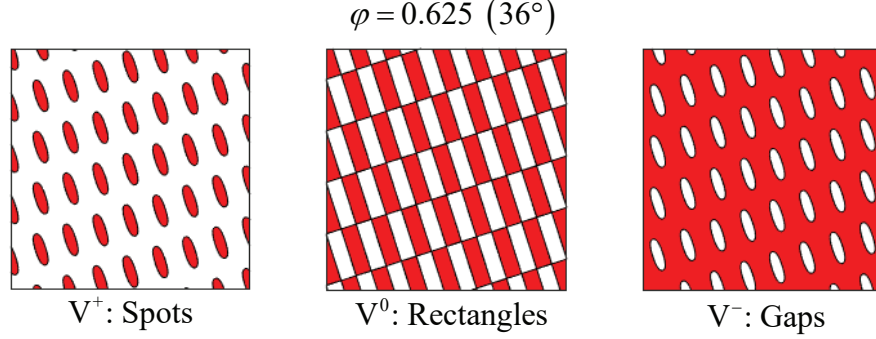
Figure 4.1: Rhombic patterns in the x-y plane relevant to $g(x,z)$ for $\varphi = 0.625\ (36°)$ with threshold values from left to right of 1, 0, and -1, which are denoted by $\mathrm{V^+}$, $\mathrm{V^0}$, and $\mathrm{V^-}$, respectively, and represent arrays of spots, rectangles, and gaps. Here, the spatial variables are being measured in units of λ_c with regions above that threshold in each part appearing red and regions below it, white. Note that $|g(x,z)| \leq 2$ and $\varphi = 0.625$ is a typical allowable rhombic angle depicted in the plot of Fig. 4.2 for $R_0 = 22$. We shall show in Section 5 that only $\mathrm{V^+}$ occurs.

Defining (Geddes *et al.*, [10])

$$\eta(R_0, \varphi) = \frac{b_1(R_0, \varphi)}{a_1(R_0)} \text{ for } R_0 > R_c, \tag{4.20}$$

we can catalogue the existence and stability criteria for the rhombic planform critical points as:

$$\text{I: } 0 < \chi < \chi_c; \text{ II: } \chi > \chi_c \text{ and } \eta > 1; \text{ V: } \chi > \chi_c \text{ and } -1 < \eta < 1. \tag{4.21}$$

Plotting η versus $\varphi \in [0, \pi]$ in Fig. 4.2 for the R_0 values of 1.762, 2, 6, 10, 14, 18, and 22, we find that there exists an interval of stable rhombic V-patterns versus stripes provided $\chi > \chi_c$, when $-1 < \eta < 1$ or $\varphi \in (\varphi_m, \varphi_M)$ where $0 < \varphi_m < \varphi_M < \pi/3$. We shall examine the sign of i_{20}, consider the possibility of the occurrence of stable striped II-patterns versus rhombic arrays, discuss the consequences of $a_1 < 0$, deduce a morphological infectious sequence in R_0, compare these theoretical predictions with relevant EIAV-horse experimental data, and conclude by offering a critique of them versus their prospective numerical simulation results in Section 5.

5   Interpretations, Applications, and Comparisons

We have deferred until now an examination of the sign of i_{20} which determines the threshold type of the rhombic arrays depicted in Fig. 4.1. Employing our previous results of Section 3,

$$i_{20} = \begin{vmatrix} 2\sigma_0 + R_0 & -1 \\ 1 - R_0 & 1 \end{vmatrix} \frac{R_0 m_{11} i_{11}}{2f(2\sigma_0; 0)}; \tag{5.1a}$$

where

$$m_{11} = \frac{\sigma_0 + q_c^2}{R_0 - 1}, \ i_{11} = 1;$$

$$f(2\sigma_0; 0) = 4\sigma_0^2 + 2R_0\sigma_0 + R_0 - 1 = (2\sigma_0 + 1)(2\sigma_0 + R_0 - 1); \tag{5.1b}$$
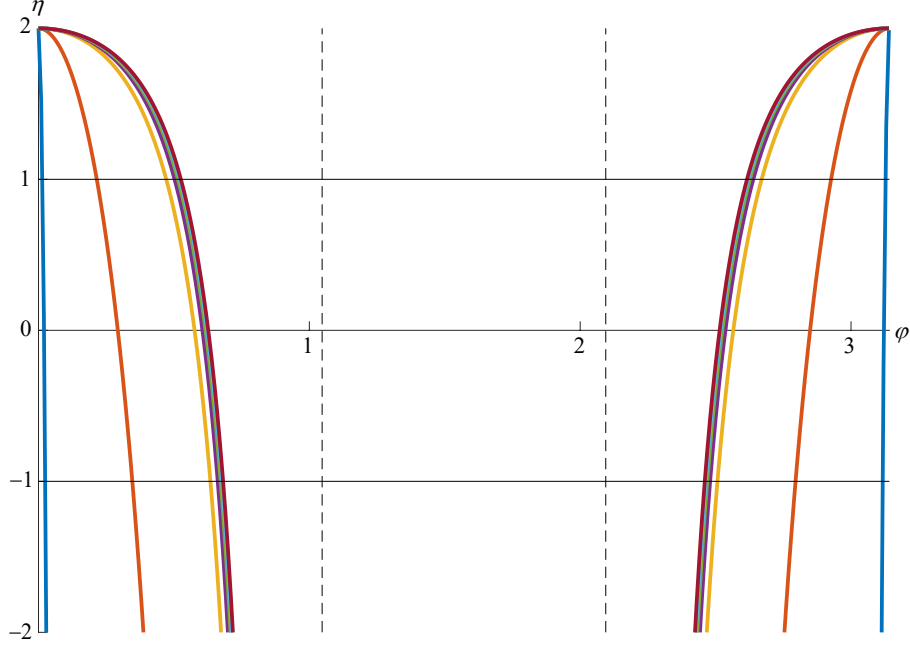
Figure 4.2: Plots of η versus $0 \leq \varphi \leq \pi/2$ from left to right for $R_0 = 1.762, 2, 6, 10, 14, 18$, and 22. Here the horizontal lines $\eta = \pm 1$ have been denoted. Observe that the curves approach an asymptotic limit with increasing R_0. This figure has been plotted for the extended angle interval $\pi/2 \leq \varphi \leq \pi$ in order to demonstrate graphically that $\eta(R_0, \varphi) = \eta(R_0, \pi - \phi)$, which when $\varphi = \pi/2 - \psi$ implies symmetry about $\pi/2$, while $\eta(R_0, 0) = 2$ or $b_1(R_0, 0) = 2a_1(R_0)$, characteristic of rhombic patterns where the first property is a consequence of modal interchange and the second, of mode interference occurring at exactly at $\varphi = 0$ (Cross and Hohenberg, [8]). Note only those rhombic angles $0 < \varphi_m < \varphi < \varphi_M < \pi/3$ where $-1 < \eta < 1$ are allowable. The vertical dotted lines designate $\varphi = \pi/3$ and its reflection through $\pi/2$ which are asymptotes.

and

$$2\sigma_0 = -2(q_c^2 + R_0) + \sqrt{(2q_c^2 + R_0)^2 + 4(R_0 - 1)\left(\frac{q_c^2}{R_0}\right)(\chi - \chi_c)} \text{ with } q_c^2(R_0) = \sqrt{R_0 - 1}.$$

Hence

$$i_{20} = i_{20}(\chi; R_0) = \frac{R_0(\sigma_0 + q_c^2)}{2(R_0 - 1)(2\sigma_0 + R_0 - 1)}. \tag{5.1c}$$

Since $\sigma_0, a_1 > 0$ for our stability analysis of critical point V in the last section, which implies that $\chi > \chi_c$ and $R_0 > R_c = 1.761 > 1$, we may now deduce that in this region of the R_0-χ plane

$$i_{20}(\chi; R_0) > 0, \tag{5.1d}$$

identically, and thus conclude that only high-threshold V^+ type-rhombic patterns of the allowable angles represented in Fig. 4.2 or the spots of Fig. 4.1 but not its gaps can occur here (see Fig.
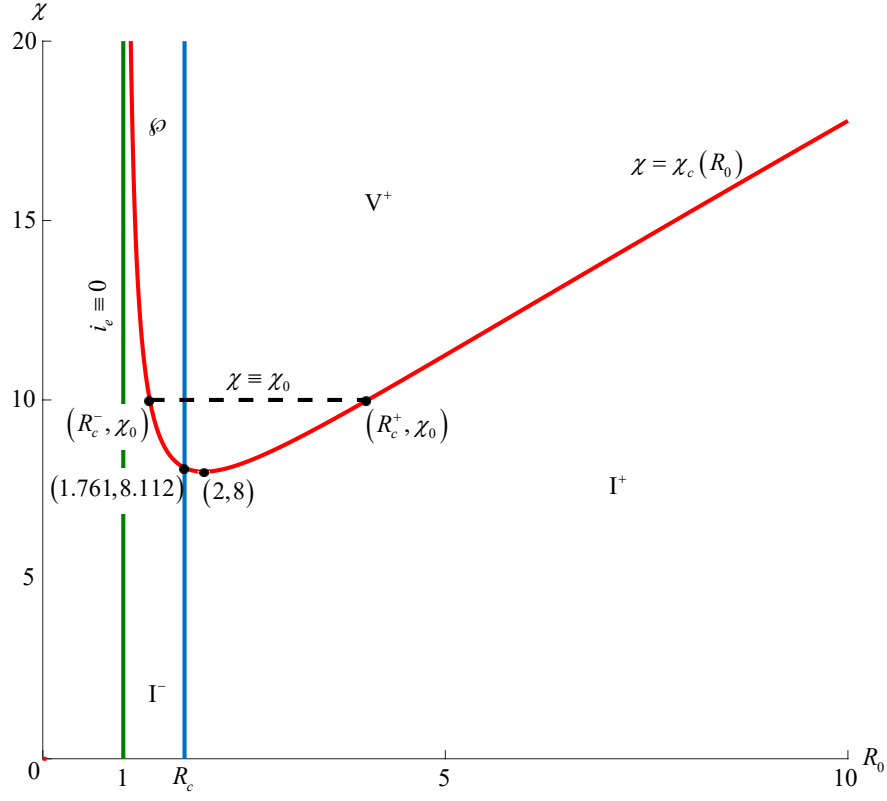
23

Figure 5.1: Plot in the R_0-χ plane modifying the linear stability results of Fig. 2.3 by virtue of our nonlinear ones. Here, the vertical line $R_0 = R_c$ on which $a_1 = 0$ separates the supercritical regime $R_0 > R_c$ where $a_1 > 0$ from the subcritical one $1 < R_0 < R_c$ where $a_1 < 0$. The horizontal line $\chi \equiv \chi_0 > \chi_c(R_c) = 8.112$ is displayed, which serves as a transit curve for the morphological infection sequence along the R_0 gradient of Table 5.1, including the intersection points with the marginal stability curve $\chi = \chi_c(R_0)$, where its R_0-components $R_c^{\pm}$ are catalogued in Table 5.2 for selected values of χ_0. Note that our generic figure has been drawn for $\chi_0 = 10$, while the morphological identifications of the regions of this plane are in accordance with those of Table 5.1. Only for the narrow range $8 < \chi_0 < 8.112$, do isolated spots $\wp$ not occur and the morphological infection sequences associated with those values transit directly from I$^-$ to V$^+$ at $R_0 = R_c^-$. Observe that, $R_c^-(8.1) = 1.692$, $R_c^+(8.1) = 2.374$; while $R_c^{\pm}(8) = 2$, the vertex of $\chi = \chi_c(R_0)$. Finally, χ_1 being difficult to measure, such a plot can be used to determine it as an inverse problem. For instance, when $R_0 = 22$, there is a transition from the I$^+$ to V$^+$ states at $\chi_c(22) = 32.649$.

5.1).

For situations of this sort, stable stripes may occur versus rhombic patterns provided there exists an $R_0 = R_k > R_c$ such that $i_{20}(\chi; R_k) = 0$ since then $b_1(R_k, \varphi) = 2a_1(R_k)$ independent of φ, in which event $b_1(R_0, \varphi)$ exhibits a jump-discontinuity at that value of R_0 (Wollkind and Dichone, [31]). Given that this is obviously not possible for us, no stable stripes can occur versus rhombic

patterns here. Despite the fact that striped patterns are predicted in this region by the longitudinal planform nonlinear stability analysis, none of them survive the rhombic planform nonlinear stability analysis, although the homogeneous distributions of critical point I do survive for their planar region of $R_0 > R_c$ and $0 < \chi < \chi_c$. In the caption of Fig. 2.3, we have designated these sparse to dense homogeneous distributions by I^- to I^+. So far, with the implicit exception of I^- in that caption, we have been considering the morphological stability behavior of our model system for $a_1 > 0$. We next consider its behavior for $a_1 < 0$.

In Wollkind and Dichone [31], it was shown that a particular partial differential lubrication equation containing fourth-order spatial derivatives could be used when $a_1 < 0$, $\sigma_0 > 0$ to explain the occurrence of dewetting of thin liquid layers by isolated droplet pattern formation for relatively thin layers and by isolated hole formation for relatively thick ones, where a fifth-order Landau coefficient $a_3 > 0$. A comparison of the simulation results of Lejeune *et al.* [15] with the weakly nonlinear stability ones of Boonkorkuea *et al.* [2] for a strongly related evolution equation describing vegetative pattern formation in arid isotropic environments led to the conjecture that when $a_1 < 0$ localized structures would occur where $\sigma_0 > 0$, characterized by isolated patches of vegetation at low densities that were a spatial compromise between the periodic patchy vegetation and bare ground stable states. Chen and Ward [7] found local structures occurring in conjunction with such subcriticality for the Gray-Scott reaction-diffusion chemical model system (Pearson, [19]). These occurrences led Cangelosi *et al.* [5] to employ the same argument to identify a region of their relevant parameter space with isolated clusters for a mussel-algae interaction-diffusion model system. The resulting morphological sequence deduced from that identification provided close agreement with mussel bed patterning observations both in the field (Wang *et al.*, [29]) and laboratory (Liu *et al.*, [16]). Given the similarity of behavior among all these phenomena, Chaiya *et al.* [6] conjectured with some confidence that isolated patches of vegetation occurred for their root suction driven plant-ground water model when both $\sigma_0 > 0$, $a_1 < 0$ and designated that pattern by using the notation $\wp$. Further, in the region where $\sigma_0, a_1 < 0$, they predicted a sparse homogeneous distribution also designated by I^- as described in what follows.

Taking into account terms through fifth-order in the expansion and amplitude equation for the longitudinal planform analysis when $a_1 < 0$, by considering $dA/dt \sim \sigma_0 A - a_1 A^3 - a_3 A^5$ and calculating a_3, we might enhance our understanding of the morphological stability of our system in its subcritical regime. As demonstrated by Davis *et al.* [9], should $a_3 > 0$ this equation will have three equilibrium points: Namely, 0 and $2a_3(A_e^\pm)^2 = \pm\sqrt{a_1^2 + 4a_3\sigma_0} - a_1$ such that 0 is globally stable for $\sigma_0 < \sigma_{-1} = -a_1^2/(4a_3) < 0$; A_e^+, for $\sigma_0 > 0$; and in the overlap bistability region $\sigma_{-1} < \sigma_0 < 0$, 0 is stable for $A^2(0) < (A_e^-)^2$ and A_e^+, for $A^2(0) > (A_e^-)^2$; while A_e^-, which only exists in that region, is not stable there. Chaiya *et al.* [6] identified these potentially stable critical points 0 and A_e^+ with their I^- and $\wp$ states, respectively. After those authors, we shall identify these potentially stable critical points with our I^- and $\wp$ states, where the latter corresponds to isolated spots of infection at low densities that are a spatial compromise between the infected rhombic V^+ periodic spotted and the uninfected stable states. Having collectively identified the infective stable patterns occurring in all the regions of the R_0-χ plane depicted in Fig. 5.1, we predict the morphological sequence tabulated below in Table 5.1 occurring along the horizontal line $\chi \equiv \chi_0 > \chi_c(R_c) = 8.112$ as $R_0 > 0$ is increased.

R_0-range	Stable pattern
$0 < R_0 < 1$	Uninfected state $i_e \equiv 0$
$1 < R_0 < R_c^-$	Sparse homogeneous I^-
$R_c^- < R_0 < R_c = 1.761$	Isolated spots $\wp$
$R_c < R_0 < R_c^+$	Periodic spots V^+
$R_0 > R_c^+$	Dense homogeneous I^+

Table 5.1: Morphological sequence along an infectious gradient for $\chi \equiv \chi_0 > \chi_c(R_c) = 8.112$, as R_0 is increased from zero identified in Fig. 5.1.

In order to complete our description of this morphological sequence it is only necessary for us to derive representations for $R_c^\pm$, the R_0-components of the points of intersection of the marginal stability curve with $\chi \equiv \chi_0 > \chi_c(R_c)$, which we can accomplish as follows: These points satisfy

$$\chi = \chi_c(R_0) = \frac{R_0^2}{R_0 - 1} + 2\frac{R_0}{\sqrt{R_0 - 1}} = \chi_0 \text{ for } R_0 > 1. \tag{5.2a}$$

Then defining

$$r_0 = \frac{R_0}{\sqrt{R_0 - 1}} > 0 \text{ for } R_0 > 1, \tag{5.2b}$$

we find that

$$r_0^2 + 2r_0 = \chi_0 \text{ for } r_0 > 0 \text{ and } \chi_0 > \chi_c(R_c). \tag{5.2c}$$

Hence

$$r_0^2 + 2r_0 + 1 = (r_0 + 1)^2 = \chi_0 + 1 \Rightarrow r_0 = (\chi_0 + 1)^{1/2} - 1. \tag{5.2d}$$

Now,

$$r_0^2 = \frac{R_0^2}{R_0 - 1} \Rightarrow R_0^2 - r_0^2 R_0 + r_0^2 = 0. \tag{5.2e}$$

Finally, $R_0 = R_c^\pm$, where

$$2R_c^\pm = r_0^2 \pm (r_0^4 - 4r_0^2)^{1/2} = r_0[r_0 \pm (r_0^2 - 4)^{1/2}] \text{ for } r_0 = (\chi_0 + 1)^{1/2} - 1 > 2, \tag{5.2f}$$

since $\chi_0 > \chi_c(R_c) > \chi_c(2) = 8$. Note, $1 < R_c^- < R_c < 2 < R_c^+$. In Table 5.2 we catalogue $R_c^\pm$.

χ_0	R_c^-	R_c^+
8.2	1.695	2.439
10.0	1.329	4.038
20.0	1.093	11.742
30.0	1.053	19.811
32.6	1.048	21.959
40.0	1.037	28.157
50.0	1.028	36.869
99.0	1.013	79.987

Table 5.2: $R_c^\pm(\chi_0)$ for some selected values of χ_0.

Here, after Chaiya *et al.* [6], we have implicitly assumed that $\chi_{\sigma_{-1}}(R_0) \cong \chi_c(R_0)$ where $\chi_{\sigma_{-1}}(R_0)$ is the $\sigma_0 = \sigma_{-1}$ generalized marginal curve in the R_0-χ plane for $R_0 < R_c$ obtained in the same way that $\chi_c(R_0)$ was for $\sigma_0 = 0$ (Wollkind and Dichone, [31]). Should that not be the case, then Table 5.1 would need to be replaced by the slightly more complicated Table 5.3 tabulated below. Note that, although this allows for the possibility of a bistability region where either I^- or $\wp$ might occur depending on initial conditions, the morphological infection sequence of Table 5.1 is essentially preserved, except for several potential hysteretical switches between these two states there. Hence, we shall describe it as a transition from an uninfected state to sparse homogeneous distributions & isolated spots to periodic spots to dense homogeneous distributions as R_0 increases from zero where the pattern wavelength of $\lambda_c = 2\pi/\sqrt[4]{R_0 - 1}$ in the periodic region decreases as R_0 increases, consistent with such a morphological infection sequence.

R_0-range	Stable pattern
$0 < R_0 < 1$	Uninfected state $i_e \equiv 0$
$1 < R_0 < R_{-1}$	Sparse homogeneous I^-
$R_{-1} < R_0 < R_c^-$	Sparse homogeneous I^- & Isolated spots $\wp$
$R_c^- < R_0 < R_c = 1.761$	Isolated spots $\wp$
$R_c < R_0 < R_c^+$	Periodic spots V^+
$R_0 > R_c^+$	Dense homogeneous I^+

Table 5.3: Morphological sequence along an infectious gradient for $\chi \equiv \chi_0 > \chi_c(R_c) = 8.112$, where $\chi_{\sigma_{-1}}(R_{-1}) = \chi_0$ with $\sigma_{-1} = -a_1^2/(4a_3) < 0$. In Table 5.1, we assumed that $R_{-1} \cong R_c^-$.

It remains to compare our theoretical predictions with EIAV veterinary medicine horse observations. Figure 5.2 is an image of petechial hemorrhages occurring on an anemic mucous membrane of a horse during the chronic degree phase of EIAV infectiousness. Here, as stated in Section 1, the patterning is caused by the mechanism of uninfected target cells being chemotactically attracted to, and moving toward, density gradients in the infected target cells since the latter recruit the former by signaling them (Jin *et al.*, [12]) through the release of chemokines (chemotactic cytokines) producing inflammation at the site of the infection which appears as these minute blood-red spotted patterns (Stancevic *et al.*, [24]). Our predicted spots $\wp$ and V^+ for $\chi > \chi_c$ and sparse and dense homogeneous states $I^\pm$ for $0 < \chi < \chi_c$ of Fig. 5.1 bear a close qualitative resemblance to those patterns. In addition to the rate parameters of Table 1.2, Schwartz *et al.* [21] reported the median value $b = 505$ viral RNA copies/(cells $\times$ day). Then for these rate parameters the horses of Table 1.2 had $R_0 = 21.70$. Given our length scale, the nondimensional wavelength λ_c defined above corresponds to the dimensional wavelength of

$$\lambda_c^* = \frac{2\pi \sqrt{D_1/\rho}}{\sqrt[4]{R_0 - 1}}, \tag{5.3}$$

or $\lambda_c^* = 4.162$ mm from Table 1.2 and b, a plausible value for distance between adjacent spots. We have considered our spatial domain to be infinite in planar extent given that this wavelength of the patterns under investigation was relatively small with respect to the territory size in question and consequently its boundary did not significantly influence those patterns (Graham *et al.*, [11]). Hence, it seemed reasonable to assume such an unbounded spatial domain as a first approximation. This is the exact analogue of employing periodic-type boundary conditions during numerical

Figure 5.2: Image of petechial hemorrhages or petechiations occurring on an anemic mucous membrane of a horse during the chronic degree phase of EIAV infectiousness (courtesy of Dr. Thomas J. Lane, Professor Emeritus, College of Veterinary Medicine, University of Florida).

simulations as opposed to the zero-flux ones adopted by Stancevic *et al.* [24].

There is one more comparison between our theoretical predictions and the experimental measurements of Schwartz *et al.* [21] we wish to include. Toward that end we now compare the quantities tabulated in Table 5.4 below, the entries of which can be explained as follows: The first two rows represent experimental measurements of two selected horses in the study of Schwartz *et al.* [21] where T_e and V_e are equilibrium numerical values for the uninfected target cell population density and viral concentration, respectively, in dimensional variables. Each entry in the third row is the arithmetic mean value of the entries in the first two rows with the exception of its third column entry in which the average of V_e is implicitly meant in the sense of the geometric mean $\sqrt{AB}$ since

$$\log_{10}(\sqrt{AB}) = \frac{1}{2}\log_{10}(AB) = \frac{\log_{10}(A) + \log_{10}(B)}{2} \text{ for } A, B > 0. \tag{5.4}$$

Finally the fourth row contains our predictions where $T_e = (1/R_0)\lambda/\rho$, $V_e = (R_0 - 1)\rho/\beta$ for $v_e = R_0 i_e = R_0 - 1$, and $R_0 = \lambda\beta b/(\rho^2\gamma) = 21.7$. Hence, from Table 1.2 and this value of R_0,

$$T_e = \frac{(2019)(21)}{21.7}\frac{\text{cells}}{\text{ml}} = 1.95 \times 10^3 \frac{\text{cells}}{\text{ml}},$$
$$V_e = \frac{20.7}{(21)(3.25 \times 10^{-7})}\frac{\text{RNA copies}}{\text{ml}} = 3.033 \times 10^6 \frac{\text{RNA copies}}{\text{ml}} \tag{5.5a}$$

$$\Rightarrow \log_{10}(3.033 \times 10^6) = 6 + \log_{10}(3.033) = 6.48. \tag{5.5b}$$

28

This self-consistency between theory and experiment as exhibited in Table 5.4 is of utmost importance in veterinary medicine and the ultimate goal of comprehensive applied mathematical modeling in both the natural and engineering sciences (Wollkind and Dichone, [30]; [31]).

Data	R_0	T_e (cells/ml)	V_e (RNA copies/ml)	$\log_{10}(V_e)$
Horse A2202	22.30	1.90×10^3	5.495×10^6	6.74
Horse A2205	21.00	2.02×10^3	1.862×10^6	6.27
Average	21.65	1.96×10^3	3.199×10^6	6.51
Predicted	21.70	1.95×10^3	3.033×10^6	6.48

Table 5.4: Comparison between experimental measurements of Schwartz *et al.* [21] and our theoretical predictions for the dimensional form of the dependent variables.

Our system is very similar to flat dryland plant-water consumer-resource models (Wollkind and Dichone, [31]) in that the latter's bare-ground state and vegetative patterns correspond to the uninfected state and infectious patterns, respectively, including sparse and dense homogeneous distributions and isolated and periodic arrays. Our Turing pattern formation mechanism as in the root-suction driven plant-ground water problem of Chaiya *et al.* [6] is again by means of a cross-diffusive effect (chemotaxis in the uninfected target cell equation) rather than by a self-diffusive one as with most Turing pattern problems in the biophysical and biochemical sciences.

In conclusion, we have performed a rhombic planform nonlinear stability analysis on the infectious state of our noncytopathic EIAV-target cell limited interaction-dispersion-chemotaxis quasi-equilibrium model system and obtained a morphological infection sequence in its basic reproductive number-chemotaxis coefficient parameter space which compares favorably with virally infected horse data. That rhombic-planform stability method, while incorporating the nonlinearities of this EIAV-target cell limited model system, basically pivots a perturbation procedure about the critical point of linear stability theory. The advantage of such an approach over strictly numerical procedures is that it allows one to deduce quantitative relationships between system parameters and stable patterns which are valuable for comparison with observational or experimental evidence and difficult to accomplish using simulation alone. Researchers who prefer these numerical techniques to weakly nonlinear ones claim that the latter are only valid in the neighborhood of the marginal stability curve in this parameter space and that simulations provide global validity. From our past experience, as described in Wollkind and Dichone [31], it has often been possible to extrapolate these weakly nonlinear stability results to regions of parameter space far removed from the marginal stability curve and that these predictions agree very well with numerical results for particular choices of parameters in those regions. Realize also that these numerical simulations must be performed for each different set of parameter values the pattern formation behavior of which one wishes to determine. Our figures in general are in the spirit of a picture being worth a thousand words, while the parameter space plot of Fig. 5.1 is in the spirit of a formula being worth a thousand pictures. Further, note that without making the requisite quasi-equilibrium approximation no such analytical results would have been possible for our unreduced EIAV model system, which was the case with Stancevic *et al.* [24], whose cytopathic HIV model system could only be handled by numerical simulations. In two-dimensions, this procedure required a regularization of the chemotaxis term in their uninfected target cell equation to prevent the occurrence of a finite-time blow up at high

chemotactic strengths, that was not an issue for our rhombic planform nonlinear stability analysis.

References

[1] Anderson, RM, May, RM (1992) Infectious diseases of humans: Dynamics and control. Oxford University Press, Oxford.

[2] Boonkorkuea, N, Lenbury, Y, Alvarado, FJ, Wollkind, DJ (2010) Nonlinear stability analyses of vegetative pattern formation in an arid environment. J. Biol.Dyn. 4, 346-380.

[3] Burg, D, Rong, L, Neumann, AU, Dahari, H (2009) Mathematical modeling of viral kinetics under immune control during primary HIV-1 infection. J. Theor. Biol. 259, 751–759.

[4] Cangelosi, RA, Schwartz, EJ, Wollkind, DJ (2018) A quasi-steady-state approximation to the basic target-cell-limited viral dynamics model with a non-cytopathic effect. Frontiers in Microbiology 9, 54:1-6.

[5] Cangelosi, RA, Wollkind, DJ, Kealy-Dichone, BJ, Chaiya, I (2015) Nonlinear stability analyses of Turing patterns for a mussel-algae model. J. Math. Biol. 70, 1249-1294.

[6] Chaiya, I, Wollkind, DJ, Cangelosi, RA, Kealy-Dichone, BJ, Rattanakul, C (2015) Vegetative rhombic pattern formation driven by root suction for an interaction-diffusion plant-ground water model system in an arid at environment. Am J. Plant Sci. 6, 1278-1300.

[7] Chen, W, Ward, MJ (2011) The stability and dynamics of localized spot patterns in the two-dimensional Gray-Scott model. SIAM J. Dyn. Syst. 10, 586 - 666.

[8] Cross, MC, Hohenberg, PC (1993) Pattern formation outside of equilibrium. Rev. Mod. Phys. 65, 851–1112.

[9] Davis, MG, Wollkind, DJ, Cangelosi., RA, Kealy-Dichone, BJ (2018) The behavior of a population interaction-diffusion equation in its subcritical regime. Involve 11, 297-310.

[10] Geddes, JB, Indik, RA, Moloney, JV, Firth, WJ (1994) Hexagons and squares in a passive nonlinear optical system. Phys. Rev. A. 50, 3471-3485.

[11] Graham, MD, Kevrekidis, IG, Asakura, K, Lauterbach, J, Krischer, K, Rotermund, H-H, Ertl, G (1994) Effects of boundaries on pattern formation: Catalytic oxidation of CO on platinum. Science 264, 80-82.

[12] Jin, T, Xu, X, Hereld, D (2008) Chemotaxis, chemokine receptors and human disease. Cytokine 44, 1-8.

[13] Keller, EF, Segel, LA (1970) Initiation of slime mold aggregation viewed as an instability. Journal of Theoretical Biology 26, 399-415.

[14] Landau, LD (1944) On the problem of turbulence. Doklady Akademii Nauk SSR 44, 339-342.

[15] Lejeune, O, Tlidi, M, Couteron, P (2002) Localized vegetation patches: A self-organized response to resource scarcity. Phys. Rev. E 66, 010901-1-010901-4.

[16] Liu Q-X, Doelman A, Rottschafer V, de Jager M, Herman PMJ, Rietkerk M, van de Koppel J (2013) Phase separation explains a new class of self-organized spatial patterns in ecological systems. PNAS, 110, 11905-11910.

[17] Matkowsky, BJ (1970) A simple nonlinear dynamic stability problem. Bull. Amer. Math. Soc. 76, 620-625.

[18] Nijhout, HF (1991) The development and evolution of butterfly wing patterns. Smithsonian Institution Press, Washington, DC.

[19] Pearson, JE (1993) Complex patterns in a simple system. Science. 261, 189-192.

[20] Phillips, AN (1996) Reduction of HIV concentration during acute infection:independence from a particular immune response. Science 271, 497-499.

[21] Schwartz, EJ, Vaidya, NK, Dorman, K, Carpender, S, Mealey, RH (2018) Dynamics of lentiviral infection in vivo in the absence of adaptive host immune responses. Virology 513, 108–113.

[22] Segel, LA (1966) Nonlinear hydrodynamic stability theory and its applications to thermal convection and curved flows. In: Non-equilibrium thermodynamics, variational techniques, and stability. Donnelly, RJ, Herman, R, Prigogine, I (eds) University of Chicago Press, Chicago, pp. 164-197.

[23] Sekimura, T, Zhu, M, Cook, J, Maini, PK, Murray, JD (1999) Pattern formation of scale cells in Lepidoptera by differential origin-dependent cell adhesion. Bull. Math. Biol. 61, 807-827.

[24] Stancevic, O, Angstmann, CN, Murray, JM, Henry, BI (2013) Turing patterns from dynamics of early HIV infection. Bull. Math. Biol. 75, 774-795.

[25] Tuckwell, HC, Wan, FYM (2004). On the behaviour of solutions in viral dynamical models. BioSystems 73, 157–161.

[26] Turing, AM (1952) The chemical basis of morphogenesis. Phil. Trans. Roy. Soc. London B 237, 37-72.

[27] Uspensky, JV (1948) Theory of equations. McGraw Hill, New York.

[28] Walgraef, D (1997) Spatio-temporal pattern formation, Springer, New York.

[29] Wang, R-H, Liu, Q-X, Sun, G-Q, Jin, A, van de Koppel, J (2009) Nonlinear dynamic and pattern bifurcations in a model for spatial patterns in young mussel beds. J. R. Soc. Interface. 6, 705-718.

[30] Wollkind, DJ, Dichone, BJ (2017) Comprehensive applied mathematical modeling in the natural and engineering sciences. Springer, Cham (Switzerland).

[31] Wollkind, DJ, Dichone, BJ (2022) Pulling rabbits out of hats. CRC Press, Boca Raton (Florida).